CELL BIOLOGY

Plakophilin-2 truncating variants impair cardiac contractility by disrupting sarcomere stability and organization

Kehan Zhang[1,2], Paige E. Cloonan[1], Subramanian Sundaram[1,2], Feng Liu[3], Shoshana L. Das[1,2,4], Jourdan K. Ewoldt[1,2], Jennifer L. Bays[1,2], Samuel Tomp[1], Christopher N. Toepfer[5,6], Júlia D. C. Marsiglia[5], Joshua Gorham[5], Daniel Reichart[5], Jeroen Eyckmans[1,2], Jonathan G. Seidman[5], Christine E. Seidman[5,7,8], Christopher S. Chen[1,2]*

Progressive loss of cardiac systolic function in arrhythmogenic cardiomyopathy (ACM) has recently gained attention as an important clinical consideration in managing the disease. However, the mechanisms leading to reduction in cardiac contractility are poorly defined. Here, we use CRISPR gene editing to generate human induced pluripotent stem cells (iPSCs) that harbor plakophilin-2 truncating variants (*PKP2*tv), the most prevalent ACM-linked mutations. The *PKP2*tv iPSC–derived cardiomyocytes are shown to have aberrant action potentials and reduced systolic function in cardiac microtissues, recapitulating both the electrical and mechanical pathologies reported in ACM. By combining cell micropatterning with traction force microscopy and live imaging, we found that *PKP2*tvs impair cardiac tissue contractility by destabilizing cell-cell junctions and in turn disrupting sarcomere stability and organization. These findings highlight the interplay between cell-cell adhesions and sarcomeres required for stabilizing cardiomyocyte structure and function and suggest fundamental pathogenic mechanisms that may be shared among different types of cardiomyopathies.

INTRODUCTION

Arrhythmogenic cardiomyopathy (ACM), previously called arrhythmogenic right ventricular cardiomyopathy/dysplasia, is a heritable disorder of cardiac muscle affecting an estimated 1 in 1000 to 1 in 5000 people and is a major cause of sudden cardiac death, particularly in young adults (*1*). ACM is characterized pathologically by fibrofatty replacement of myocardium and clinically by prominent ventricular arrhythmias, ventricular dilation, and decreased systolic function (*1*, *2*). In the past decade, genetic characterization of ACM has revealed that more than half of documented cases are associated with pathogenic variants in genes encoding desmosomal proteins, of which the most commonly mutated gene is *PKP2*, which encodes the protein plakophilin-2 (PKP2) (*3*, *4*).

Recent efforts have focused on the mechanisms by which pathogenic variants in desmosomal genes might cause pathological and clinical features of ACM. Studies investigating the relationship between defective PKP2 and arrhythmias have demonstrated a role for PKP2 in regulating gap junction formation, sodium channel function, and intracellular calcium cycling (*5*–*12*). Signaling pathways including canonical and noncanonical Wnt signaling, the Hippo–Yes-associated protein (YAP) pathway, and transforming growth factor-β signaling have been shown to be involved in the fibrofatty deposition caused by *PKP2* pathogenic variants (*9*, *13*–*16*). In contrast to these advances, relatively little attention has been given to the mechanisms by which pathogenic variants in desmosomal genes lead to the ventricular dilation and decreased systolic function associated with ACM.

Desmosomes are a type of intercellular junction that connect intermediate filaments in neighboring cardiomyocytes (CMs), providing structural and mechanical integrity to cardiac muscle (*17*). On the basis of the role of desmosomes in mechanically coupling CMs, it has been postulated that pathogenic variants in desmosomal genes lead to weakened adhesion between CMs and a resulting predisposition to injury and detachment during contraction, thereby triggering secondary mechanisms such as CM loss, compensatory fibrosis, progressive ventricular dilation, and decreased systolic function (*3*). Earlier studies demonstrated decreased cell-cell adhesion in cultures of epithelial or HL-1 CM–like cells following knockdown of desmosomal genes or overexpression of ACM-causing mutations (*18*). Whether these decreases in cell-cell adhesion affect CM health or contractile function remains uncertain. Characterizing these biophysical mechanisms in specialized engineered platforms using cultured cells was problematic until recently (*19*–*22*).

Advances in human induced pluripotent stem cell (iPSC) technology, including efficient differentiation of iPSCs into CMs (iPSC-CMs), have provided a new source of human CMs to study clinically relevant mutations. Patient-derived iPSC-CMs harboring patient-specific gene variants serve as a good system for disease modeling with iPSC-CMs generated from healthy probands frequently used as controls for experiments (*23*–*25*). However, this approach is of limited use for establishing causal relationship between specific mutations and functional phenotypes because different iPSC lines have different genetic backgrounds. Recently, CRISPR-mediated genome editing technology has generated considerable excitement with its efficiency and reliability to make precise, targeted changes

[1]Department of Biomedical Engineering, Boston University, Boston, MA 02215, USA. [2]Wyss Institute for Biologically Inspired Engineering, Harvard University, Boston, MA 02115, USA. [3]State Key Laboratory of Nonlinear Mechanics, Institute of Mechanics, Chinese Academy of Sciences, Beijing 100190, China. [4]Harvard-MIT Program in Health Sciences and Technology, Institute for Medical Engineering and Science, Massachusetts Institute of Technology, Cambridge, MA 02139, USA. [5]Department of Genetics, Harvard Medical School, Boston, MA 02115, USA. [6]Division of Cardiovascular Medicine, Radcliffe Department of Medicine, University of Oxford, Oxford OX3 9DU, UK. [7]Division of Cardiovascular Medicine, Brigham and Women's Hospital, Boston, MA 02115, USA. [8]Howard Hughes Medical Institute, Chevy Chase, MD 20815, USA.
*Corresponding author. Email: chencs@bu.edu

to the genome of living cells and has allowed for the generation of isogenic controls and patient-specific mutations in iPSC-CMs. This approach creates an experimental model that is ideally controlled for in vitro modeling of various cardiomyopathies, shedding new light on molecular mechanisms contributing to the pathogenesis of diseases (*26*–*29*).

In this work, we harness these recent advances in human iPSC, CRISPR gene editing, and engineered culture platforms to develop a model of ACM with *PKP2* truncating variants (*PKP2*tvs), the most prevalent type of pathogenic variants in ACM. CMs differentiated from these *PKP2*tv-harboring iPSCs recapitulated aberrant expression and localization of junctional components and electrical features that are characteristic of ACM. We then show that *PKP2*tvs also impair cardiac tissue contractility, recapitulating systolic dysfunction observed in ACM. Furthermore, we delve into the pathogenic mechanisms underlying systolic dysfunction and uncover that PKP2 truncations lead to impaired force generation in multicellular syncytia by destabilizing cell-cell junctions and in turn disrupting sarcomere stability and organization.

RESULTS

CRISPR-engineered human iPSC-CMs with *PKP2*tvs demonstrate electrical and mechanical aberrations characteristic of ACM

Truncating variants in the *PKP2* gene represent 70 to 90% of all PKP2 variants associated with ACM (*30*–*32*). Pathogenic truncations at the head domain of PKP2, such as p.R79X and p.Q133X, have been reported in the literature in multiple individuals and families affected with ACM (*33*). To mimic these pathogenic variants, we used CRISPR-Cas9–mediated gene editing to create isogenic iPSC models of PKP2 truncations using wild-type (WT) cell lines from two different donors (WT1 and WT2). The engineered mutant iPSC lines with *PKP2*tvs, including a heterozygous line (*PKP2*tv$^{+/-}$) from WT1 and a homozygous line (*PKP2*tv$^{-/-}$) from WT2, contained a 5–base pair (bp) deletion according to MiSeq sequencing (Fig. 1A), predicting an early truncation of the protein (PKP2 p.D109Afs*10) that mimics the patient variants (Fig. 1B). These mutant iPSCs could be differentiated into CMs that stained positive for sarcomeric α–actinin-2 (Fig. 1C), suggesting that PKP2 is not critical for the differentiation of CMs.

To validate whether the CRISPR-edited mutant iPSC-CMs can recapitulate phenotypic features of ACM, we first assessed the expression and localization of junctional components that are affected in ACM (*34*). RNA expression of *PKP2* gene is reduced to 63.2 ± 13.9% (means ± SEM) in *PKP2*tv$^{+/-}$ compared to WT1 and 32.5 ± 6.2% (means ± SEM) in *PKP2*tv$^{-/-}$ compared to WT2 (Fig. 1D). Immunofluorescence staining and Western blot showed that PKP2 protein expression was significantly reduced in *PKP2*tv$^{+/-}$ and was almost absent in the *PKP2*tv$^{-/-}$ iPSC-CMs (Fig. 1, C to F). The reduced expression and junctional localization of PKP2 had no significant impact on the formation of adherens junctions as indicated by N-cadherin localization to cell-cell contact (Fig. 2, A to C). In contrast, *PKP2*tv did reduce junctional localization of desmoplakin (Fig. 2, A and D), a protein that links the membrane desmosome complex to the desmin intermediate filament, suggesting an impaired connection between the desmosome junctions and the cytoskeleton. Impaired desmosomal junctions have been found to affect gap junctions and, hence, may contribute to the characteristic arrhythmogenicity associated with ACM (*5*, *34*). Consistent with these reports, we observed a significant decrease in the junctional intensity of connexin-43 (Cx43) by immunofluorescence staining in the

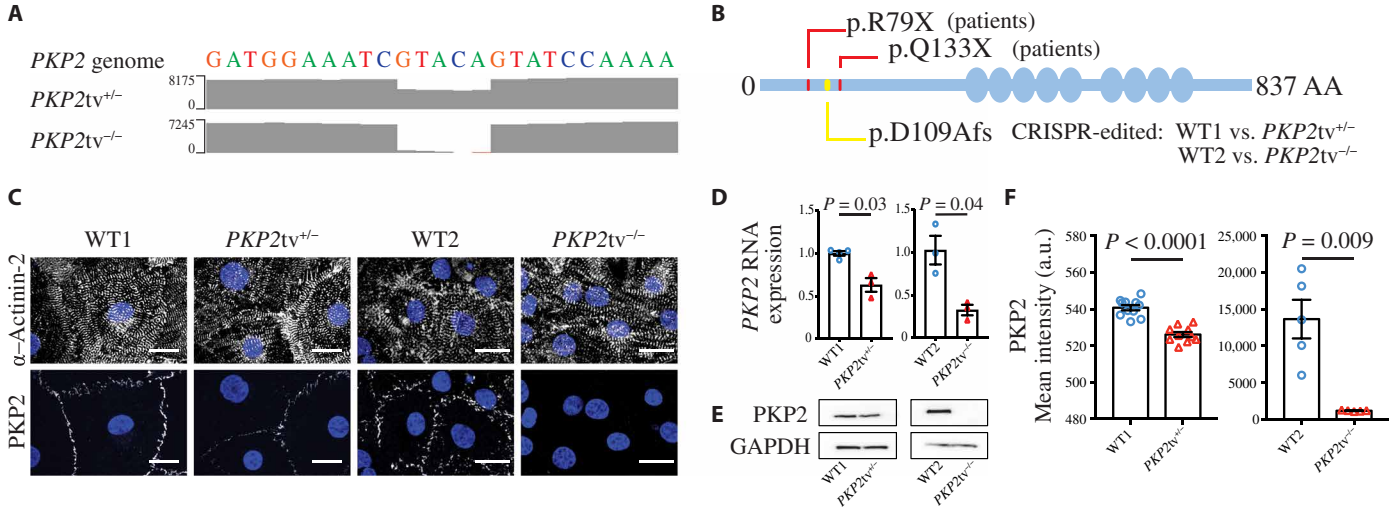

Fig. 1. CRISPR-engineered human iPSC-CMs with *PKP2*tvs demonstrate decreased expression of PKP2. (**A**) MiSeq readout aligned to the reference *PKP2* genome shows 5-bp deletion at the end of exon2 in the *PKP2*tv$^{+/-}$ and *PKP2*tv$^{-/-}$ cell lines. (**B**) Schematic representation of PKP2 protein showing the location of patient mutations p.R79X and p.Q133X, and the CRISPR-engineered mutation p.D109Afs in two WT iPSC lines (WT1 versus *PKP2*tv$^{+/-}$ and WT2 versus *PKP2*tv$^{-/-}$). AA, amino acid. (**C**) Representative images of iPSC-CM monolayers fixed and stained for nuclei (blue), α–actinin-2 (gray; top), and PKP2 (gray; bottom). PKP2 fluorescence is not detectable in *PKP2*tv$^{-/-}$. Scale bars, 20 μm. (**D**) Relative RNA expression of *PKP2* gene ($2^{-\Delta\Delta CT}$) in iPSC-CMs measured by reverse transcription quantitative polymerase chain reaction (PCR): 63.2 ± 13.9% in *PKP2*tv$^{+/-}$ ($n = 4$) compared to WT1 ($n = 3$) and 32.5 ± 6.2% in *PKP2*tv$^{-/-}$ ($n = 3$) compared to WT2 ($n = 3$), data presented as means ± SEM. (**E**) Western blots of PKP2 protein in iPSC-CMs. GAPDH, glyceraldehyde-3-phosphate dehydrogenase. (**F**) Mean fluorescence intensity of junctional PKP2 shows a significant reduction in *PKP2*tv$^{+/-}$ ($n = 10$) versus WT1 ($n = 11$) and in *PKP2*tv$^{-/-}$ ($n = 5$) versus WT2 ($n = 5$). a.u., arbitrary units. Statistics: Individual data points across three independent experiments are shown with means ± SEM on plots; Student's *t* test, $\alpha = 0.05$. Immunostains are representative of at least three independent experiments.

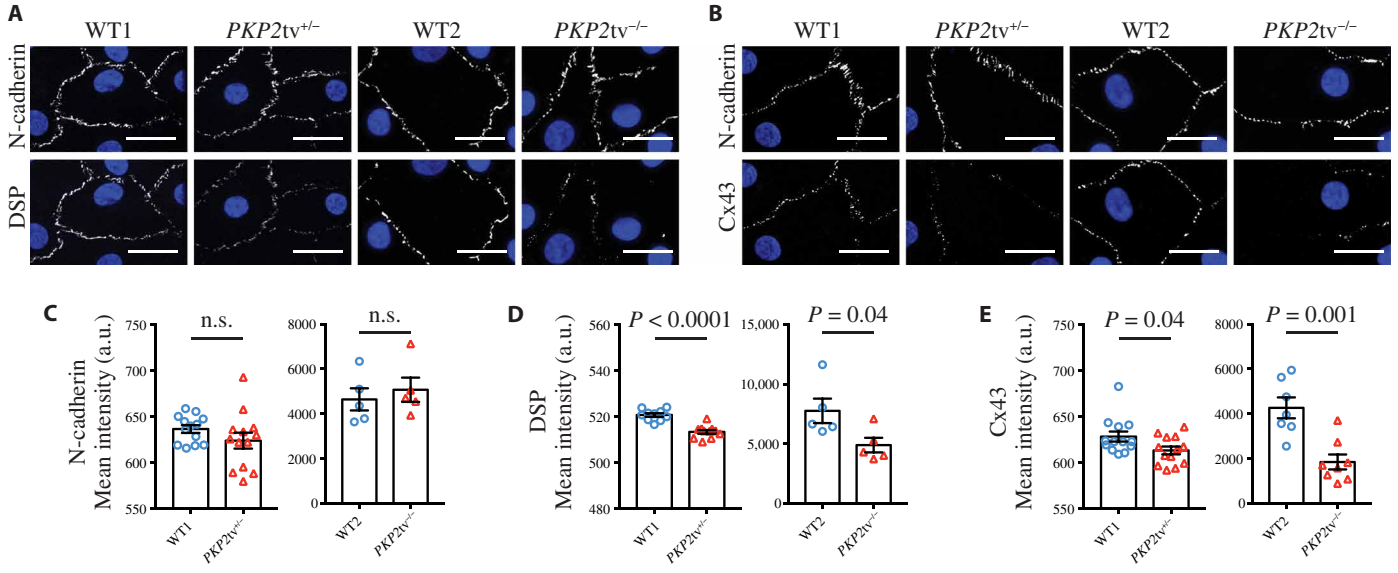

Fig. 2. *PKP2*tvs result in decreased junctional localization of desmoplakin and Cx43. (**A**) Representative images of iPSC-CM monolayers fixed and stained for nuclei (blue), N-cadherin (gray; top), and desmoplakin (DSP; gray; bottom). Scale bars, 20 μm. (**B**) Representative images of iPSC-CM monolayers fixed and stained for nuclei (blue), N-cadherin (gray; top), and Cx43 (gray; bottom). Scale bars, 20 μm. (**C**) Mean fluorescence intensity of junctional N-cadherin is comparable in *PKP2*tv$^{+/-}$ ($n = 13$) versus WT1 ($n = 13$) and in *PKP2*tv$^{-/-}$ ($n = 5$) versus WT2 ($n = 5$). n.s., not significant. (**D**) Mean fluorescence intensity of junctional desmoplakin at cell-cell contacts (defined by junctional N-cadherin signal) is significantly lower in *PKP2*tv$^{+/-}$ ($n = 11$) versus WT1 ($n = 10$) and in *PKP2*tv$^{-/-}$ ($n = 5$) versus WT2 ($n = 5$). (**E**) Mean fluorescence intensity of junctional Cx43 at cell-cell contacts (defined by junctional N-cadherin signal) is significantly lower in *PKP2*tv$^{+/-}$ ($n = 13$) versus WT1 ($n = 13$) and in *PKP2*tv$^{-/-}$ ($n = 8$) versus WT2 ($n = 7$). Statistics: Individual data points across three independent experiments are shown with means ± SEM on plots; Student's *t* test, $\alpha = 0.05$. Immunostains are representative of at least three independent experiments.

iPSC-CMs harboring *PKP2*tv$^{+/-}$ and *PKP2*tv$^{-/-}$, as compared to the WT1 and WT2 cells, respectively (Fig. 2, B and E).

Given that desmosomal mutations and knockdown of PKP2 are known to cause abnormal action potentials (*6*, *8*, *35*, *36*), we next set out to assess action potential characteristics in the iPSC lines. We expressed Archon1, a genetically encoded voltage indicator (*37*, *38*), in the cell lines and observed a significant prolongation of action potential duration (APD) in monolayer cultures of iPSC-CMs with *PKP2*tv$^{+/-}$ or *PKP2*tv$^{-/-}$, while the cells were being electrically stimulated at 1 Hz as compared to the WT1 and WT2 cells, respectively (Fig. 3, A to D). Prolonged APD is associated with early afterdepolarizations, a major type of arrhythmogenic mechanism at the cellular level (*39*, *40*), and is consistent with the phenotypes observed in ACM.

Having established CRISPR-engineered iPSC-CMs with *PKP2*tvs that present junctional and electrical abnormalities characteristic of those described in ACM and in previous cellular models of ACM, we asked whether our model also recapitulated the mechanical changes observed in ACM, such as systolic dysfunction. To study the mechanical consequences of PKP2 truncations in a biomimetic context, we generated three-dimensional (3D) cardiac microtissues (CMTs) in a previously developed process wherein cells suspended in fibrin within microwells reorganize over the course of days into aligned tissues bridging two micropillars within the microwells (Fig. 4A) (*41*, *42*). Using this model, we can measure contractile forces generated by the CMTs by tracking micropillar deflections (Fig. 4B). To eliminate any potential confounding impacts from the arrhythmogenic nature of these mutant cells, we paced the CMTs to beat at 1 Hz using an external electrical field stimulator during contractile force measurements. We observed no difference in the duration of contraction or relaxation comparing the *PKP2*tv with the WT (fig. S1, A to D), suggesting that exogenous electrical field stimulation is effective for normalizing the contraction/relaxation kinetics and eliminating potential impacts caused by aberrant electrical properties of *PKP2*tv cells. CMTs expressing *PKP2*tv$^{+/-}$ or *PKP2*tv$^{-/-}$ exhibited significantly lower systolic force or stress compared to CMTs made of WT1 or WT2 iPSC-CMs, respectively (Fig. 4, C and D). Together, these data suggest that the CRISPR-engineered iPSC-CMs harboring *PKP2*tvs can be used not only to model and study the electrical abnormalities associated with ACM but also to potentially gain insights about the nature of systolic dysfunction.

*PKP2*tvs impair force generation only in multicellular contexts

Despite increasing clinical attention on the progressive loss of ventricular systolic function in patients with ACM (*43*), little is known about how *PKP2* pathogenic variants result in reduced systolic function. To answer this question, we first assessed whether the iPSC-CMs harboring *PKP2*tvs, which exhibited compromised systolic force generation in the context of CMTs, exhibit a cell autonomous contractility defect when cultured as single cells. Because sarcomere alignment and contractility can be dictated by cell geometry (*44*, *45*), we used substrates micropatterned with rectangular extracellular matrix (ECM)–coated islands where individual cells could elongate in a controlled fashion (Fig. 5A). To measure cell-generated forces, we generated these micropatterns on elastic polyacrylamide (PAA) substrates that deform in response to cell contractions. After seeding, cells were allowed to spread, and contractility was measured after 7 days (Fig. 5B). Unexpectedly,

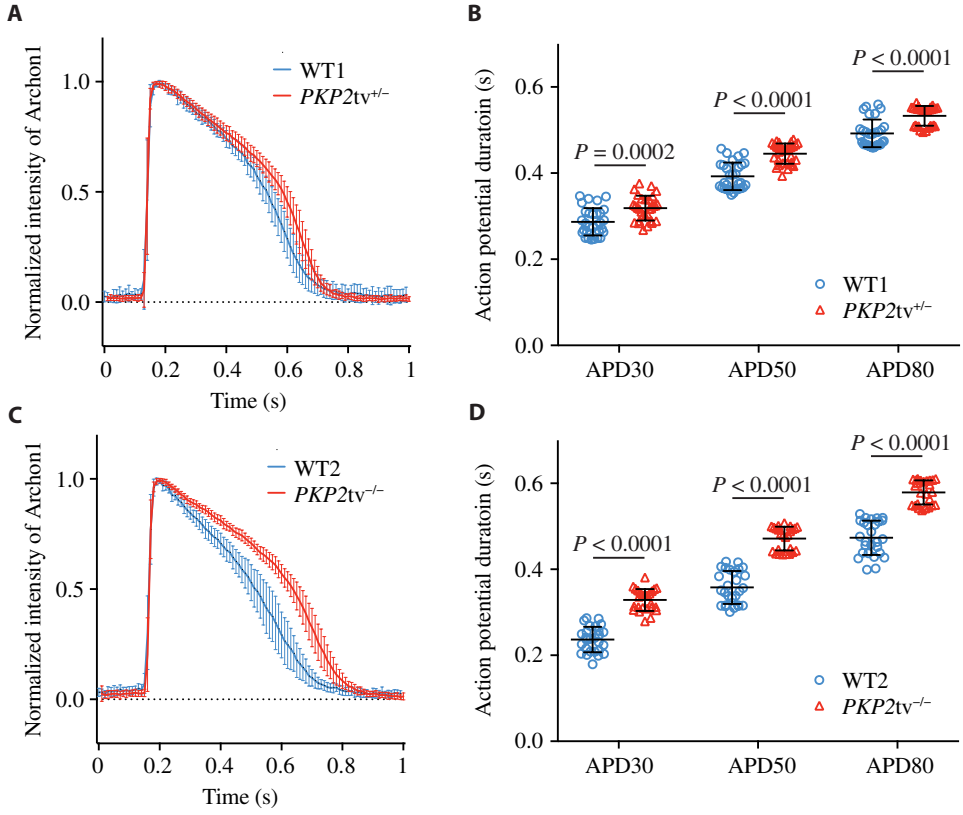

Fig. 3. *PKP2*tvs lead to prolongation of action potential. (**A** and **C**) Action potential traces of iPSC-CMs expressing Archon1 measured by normalized Archon1 fluorescence intensity, while iPSC-CM monolayers are electrically paced at 1 Hz. Data are shown as means (solid lines) ± SD (bars), and curves are aligned at peaks for (A) *PKP2*tv$^{+/-}$ ($n = 30$) versus WT1 ($n = 30$) and (C) *PKP2*tv$^{-/-}$ ($n = 27$) versus WT2 ($n = 25$). (**B** and **D**) Quantification of APD at 30, 50, and 80% below the peak of action potential curve (APD30, APD50, and APD80) shows significant increase in APD of (B) *PKP2*tv$^{+/-}$ ($n = 30$) versus WT1 ($n = 30$) and (D) *PKP2*tv$^{-/-}$ ($n = 27$) versus WT2 ($n = 25$). Statistics: Individual data points across three independent experiments are shown with means ± SEM on plots, unless otherwise specified; Student's *t* test, $\alpha = 0.05$.

single iPSC-CMs with *PKP2*tvs generated higher systolic stress and work as compared to the WT single cells (Fig. 5, C to E), suggesting that *PKP2*tvs do not cause systolic dysfunction through reducing the contractility of single CMs.

Given the opposite effects of *PKP2*tvs on contractility seen in the CMTs (Fig. 4, C and D) versus single CMs (Fig. 5, C to E), we hypothesized that *PKP2*tvs cause reduction in contractility only in multicellular structures, where cell-cell adhesion is required for establishing a mechanically coupled ensemble. To address this hypothesis, we fabricated traction force microscopy (TFM) substrates micropatterned with larger ECM islands (Fig. 6A) in which multiple CMs attach and form a 2D multicellular patch (Fig. 6B). We then evaluated the systolic stresses generated by iPSC-CMs harboring *PKP2*tvs in these multicellular structures (Fig. 6C). We observed a significant reduction in systolic stress and work generated by the cardiac patches harboring *PKP2*tvs as compared to WT controls (Fig. 6, C to E), suggesting the possibility that *PKP2*tvs impair contractility in settings that involve the presence of cell-cell adhesions.

*PKP2*tvs alter junctional N-cadherin stability and dynamics

In addition to desmosomes, adherens junctions are another major class of junctions that define the mechanical linkage between neighboring CMs, in this case coupling the sarcomere-containing myofibrils between neighboring cells. Recent studies suggest that desmosomal molecules are not restricted to the desmosome junctions but can also be detected in adherens junctions in the heart, forming a mixed-type junction referred to as area composita (*46*, *47*), which motivated us to examine the impact of *PKP2*tvs on adherens junctions. While desmosomes are compromised by *PKP2*tv (Figs. 1, C and F, and 2, A and D), adherens junctions are still present in the iPSC-CMs harboring *PKP2*tvs as indicated by N-cadherin at cell-cell adhesions (Fig. 2, A to C). This observation is consistent with biopsy and autopsy reports on the hearts of patients with ACM showing that N-cadherin–containing junctions between CMs are maintained across a range of disease phenotypes (*34*). Although N-cadherin is present, the compromised force generation seen in multicellular patches (Fig. 6, C to E) led us to posit that *PKP2*tvs might alter N-cadherin junction stability. We first used fluorescence recovery after photobleaching (FRAP) to assess whether the dynamics of N-cadherin junction remodeling is affected in *PKP2*tv (Fig. 7A and movies S1 to S4). The iPSC-CMs were infected with lentiviral constructs containing fluorescent protein–tagged N-cadherin [N-cadherin–EGFP (enhanced green fluorescent protein) or N-cadherin–mApple] and cultured in monolayer. The fluorescence intensity of junctional N-cadherin at cell-cell contact after photobleaching was imaged every 30 s for 30 min and calculated as percentage of the fluorescence intensity before photobleaching. The fluorescence recovery curve was fitted using a two-phase association model with a fast-phase and a slow-phase exponential signal recovery (Fig. 7B). The fitted

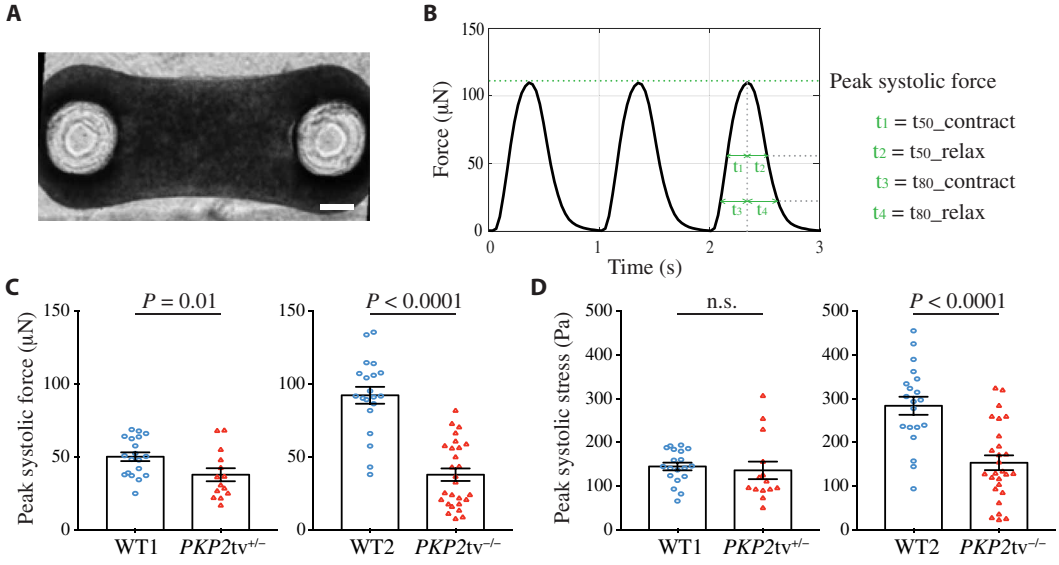

Fig. 4. *PKP2*tvs cause reduction in systolic contractility in CMTs. (**A**) Top view of a CMT suspended between two elastic polydimethylsiloxane (PDMS) pillars with spherical caps at day 10 after seeding. Scale bar, 200 μm. (**B**) Representative force-over-time curve measured from a CMT made with WT2 cells, while the tissue is electrically paced at 1 Hz. (**C**) Quantification of peak systolic forces of CMTs shows a significant reduction in force generation in *PKP2*tv$^{+/-}$ ($n = 22$) versus WT1 ($n = 25$) and in *PKP2*tv$^{-/-}$ ($n = 27$) versus WT2 ($n = 20$). (**D**) Quantification of peak systolic stresses of CMTs shows comparable stress levels in *PKP2*tv$^{+/-}$ ($n = 22$) versus WT1 ($n = 25$) and a significant reduction of systolic stress in *PKP2*tv$^{-/-}$ ($n = 27$) versus WT2 ($n = 20$). Statistics: Individual data points across three independent experiments are shown with means ± SEM on plots; Student's *t* test, $\alpha = 0.05$.

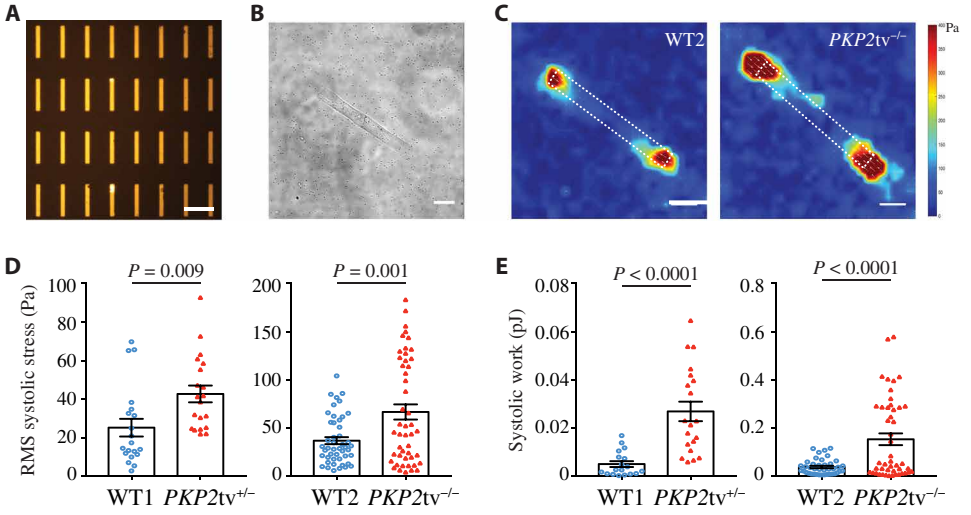

Fig. 5. Single CMs harboring *pkp2*tvs exhibit increased contractility. (**A**) Representative image of PAA gel surface micropatterned with rectangular islands of fluorescently labeled fibronectin (FN–555 nm; shown in orange). Each fibronectin island has a 1:7 aspect ratio with an area of 2000 μm^2 and allows a single CM to attach and spread on it when seeding density is properly controlled. Scale bar, 100 μm. (**B**) Representative phase image of a single iPSC-CM spread on a rectangular fibronectin island on PAA gel surface. Scale bar, 20 μm. (**C**) Representative stress vector maps at the peak systole of single CMs from traction force microscopy (TFM) measurements comparing *PKP2*tv$^{-/-}$ with WT2. Boundaries of cell area/fibronectin island are marked by white dotted lines. Scale bars, 20 μm. (**D**) Quantification of root mean square (RMS) stress at peak systole of single CM contractions shows a significantly higher stress level in *PKP2*tv$^{+/-}$ ($n = 20$) versus WT1 ($n = 20$) and in *PKP2*tv$^{-/-}$ ($n = 48$) versus WT2 ($n = 47$). (**E**) Quantification of work at peak systole of single CM contractions shows a significantly higher work production in *PKP2*tv$^{+/-}$ ($n = 20$) versus WT1 ($n = 20$) and in *PKP2*tv$^{-/-}$ ($n = 48$) versus WT2 ($n = 47$). Statistics: Individual data points across three independent experiments are shown with means ± SEM on plots; Student's *t* test, $\alpha = 0.05$.

recovery curves showed a clear separation between the *PKP2*tv and the WT cells with significantly lower mobile fraction of N-cadherin (plateau of the recovery curve) in both *PKP2*tv cell lines (Fig. 7, B and C), suggesting that a smaller pool of N-cadherin is available for junction remodeling in monolayer cultures of *PKP2*tv cells compared to the WT cells. Overall, the FRAP data suggested that the molecular stability of junctional N-cadherin is impaired by *PKP2*tv.

To visualize the stability of junctions at the cellular scale and over longer time scales, we performed time-lapse imaging on monolayer cultures of iPSC-CMs expressing the fluorescence-tagged N-cadherin every 10 min for several hours (Fig. 8, A and B, and movies S5 to S8). The time-lapse imaging revealed a more actively moving and migrating cell-cell boundary in monolayer cultures of *PKP2*tv cells compared to the WT cells. To quantify and characterize

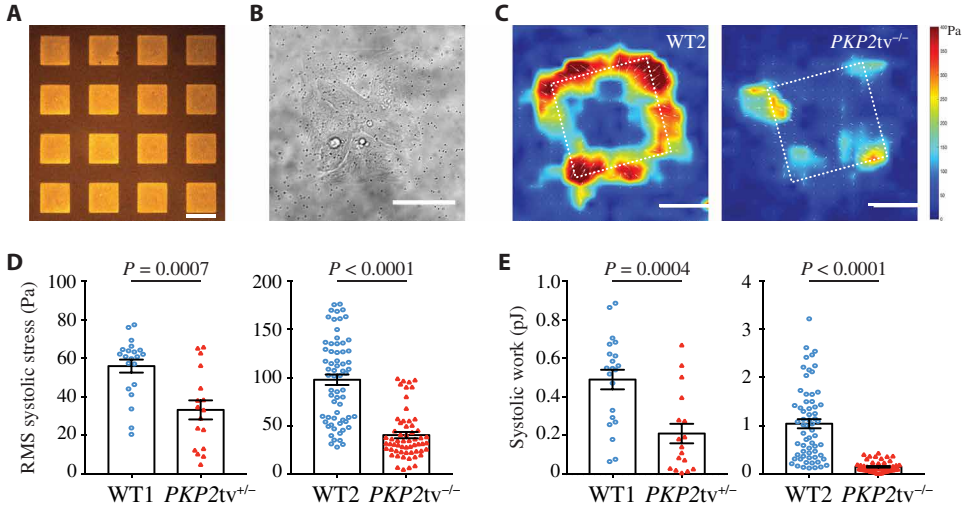

Fig. 6. *PKP2*tvs impair multicellular cardiac contractility. (**A**) Representative image of PAA gel surface micropatterned with square islands of fluorescently labeled fibronectin (FN–555 nm; shown in orange). Each fibronectin island is 100 μm by 100 μm and allows around six to eight CMs to attach and form a multicellular cardiac patch on it when seeding density is properly controlled. Scale bar, 100 μm. (**B**) Representative phase image of a cardiac patch formed by multiple iPSC-CMs spread on a square fibronectin island on PAA gel surface. Scale bar, 50 μm. (**C**) Representative stress vector maps at the peak systole of cardiac patches from TFM measurements comparing *PKP2*tv$^{-/-}$ with WT2. Boundaries of cardiac patch area/fibronectin island are marked by white dotted lines. Scale bars, 50 μm. (**D**) Quantification of RMS stress at peak systole of cardiac patches shows a significantly lower stress level in *PKP2*tv$^{+/-}$ ($n = 17$) versus WT1 ($n = 21$) and in *PKP2*tv$^{-/-}$ ($n = 59$) versus WT2 ($n = 65$). (**E**) Quantification of work at peak systole of cardiac patches shows a significantly lower work production in *PKP2*tv$^{+/-}$ ($n = 17$) versus WT1 ($n = 21$) and in *PKP2*tv$^{-/-}$ ($n = 51$) versus WT2 ($n = 64$). Statistics: Individual data points across three independent experiments are shown with means ± SEM on plots; Student's *t* test, $\alpha = 0.05$.

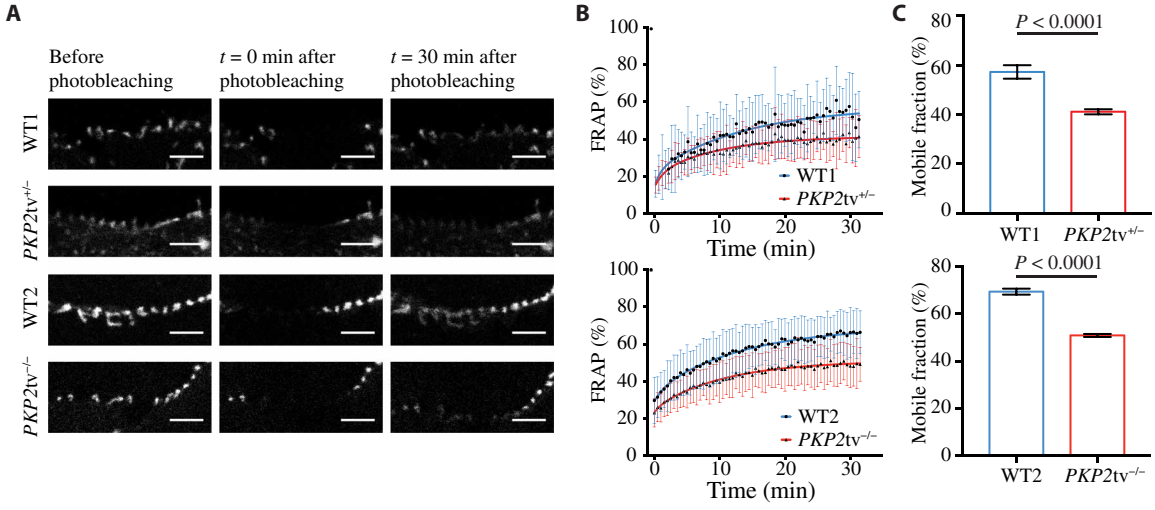

Fig. 7. *PKP2*tvs alter molecular stability and turnover of junctional N-cadherin. (**A**) Representative images of junctional N-cadherin before, right after, and 30 min after photobleaching in monolayer cultures of iPSC-CMs. Scale bars, 5 μm. (**B**) Percentage junctional N-cadherin FRAP over 30 min in monolayer cultures of iPSC-CMs comparing *PKP2*tv$^{+/-}$ ($n = 12$) versus WT1 ($n = 12$) and *PKP2*tv$^{-/-}$ ($n = 25$) versus WT2 ($n = 19$). Data are shown as means (dots) ± SD (bars) with the solid lines showing data fitted in a two-phase association model. (**C**) Mobile fraction of junctional N-cadherin measured as the plateau of FRAP recovery curves shows a significant reduction in monolayer cultures of *PKP2*tv$^{+/-}$ ($n = 12$) versus WT1 ($n = 12$) and in *PKP2*tv$^{-/-}$ ($n = 25$) versus WT2 ($n = 19$). Data across three independent experiments are shown as means ± SEM; Student's *t* test, $\alpha = 0.05$.

the dynamic movement of junctional N-cadherin at cell-cell contact, we developed a software implementing motion estimation with optical flow tracking to calculate the net displacement, mean displacement per frame, and ramble motion for the time-lapse movies (fig. S2). Quantification of junctional N-cadherin motion shows a significant increase in the net displacement of junctional N-cadherin after 8 hours of live imaging and a significant increase in the mean displacement per frame in monolayer cultures of *PKP2*tv cells compared to the WT cells, while ramble motion is not significantly different between the *PKP2*tv$^{+/-}$ and WT1 cells (Fig. 8, C to E). Together, these quantitative measurements confirmed our qualitative observations that *PKP2*tv monolayers exhibited substantially higher movement of cell-cell boundaries relative to WT monolayers.

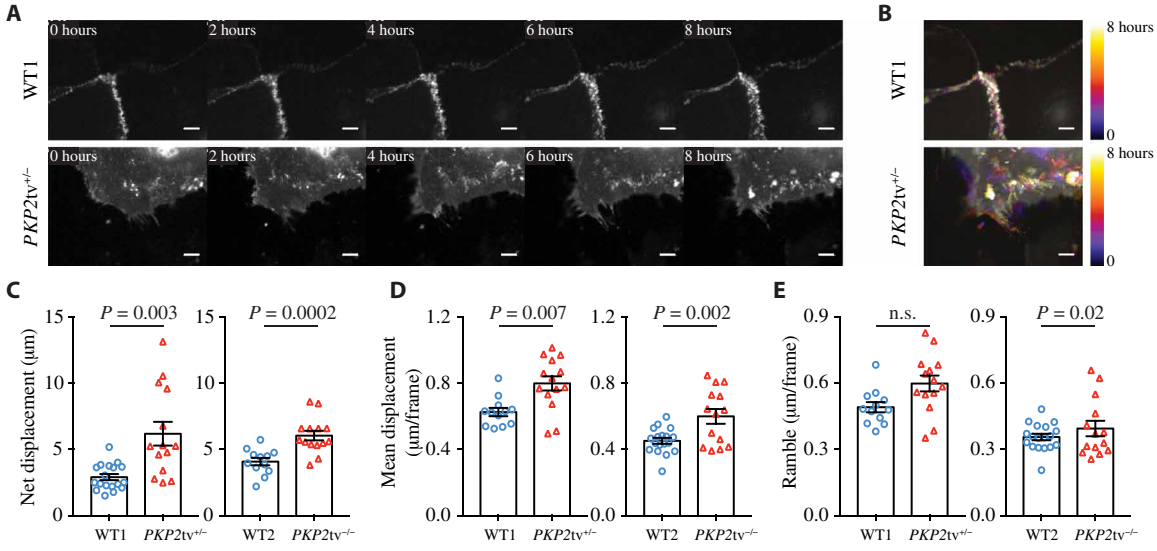

Fig. 8. *PKP2*tvs destabilize N-cadherin junctions at cell-cell contact. (**A**) Representative time-lapse images of N-cadherin junctions at 0, 2, 4, 6, and 8 hours into the live imaging of monolayer cultures of iPSC-CMs comparing *PKP2*tv$^{+/-}$ versus WT1. Scale bars, 10 μm. (**B**) Temporal color-coded hyperstacks of representative N-cadherin time-lapse movies showing stable N-cadherin junctions in monolayer cultures of WT1 and unstable cell-cell contact in *PKP2*tv$^{+/-}$. Scale bars, 10 μm. (**C**) Net displacement of junctional N-cadherin in time-lapse movies measured by optical flow tracking shows a significant increase in monolayer cultures of *PKP2*tv$^{+/-}$ ($n = 14$) versus WT1 ($n = 18$) and in *PKP2*tv$^{-/-}$ ($n = 14$) versus WT2 ($n = 12$). (**D**) Mean displacement per frame of junctional N-cadherin in time-lapse movies measured by optical flow tracking shows a significant increase in monolayer cultures of *PKP2*tv$^{+/-}$ ($n = 14$) versus WT1 ($n = 18$) and in *PKP2*tv$^{-/-}$ ($n = 14$) versus WT2 ($n = 12$). (**E**) Ramble of junctional N-cadherin in time-lapse movies measured by optical flow tracking shows an increase in monolayer cultures of *PKP2*tv$^{+/-}$ ($n = 14$) versus WT1 ($n = 18$) (not significant) and in *PKP2*tv$^{-/-}$ ($n = 14$) versus WT2 ($n = 12$) (significant). Statistics: Individual data points across three independent experiments are shown with means ± SEM on plots; Student's *t* test, $\alpha = 0.05$.

*PKP2*tvs impair sarcomere stability, content, and organization

Alterations in sarcomeres, the fundamental contractile units within CMs, have been observed in dilated cardiomyopathy (DCM) and hypertrophic cardiomyopathy (HCM) that lead to contractility changes (*48*, *49*). Since cell-cell adhesions have been shown to elicit sarcomere formation (*50*), we asked whether the altered junctional N-cadherin dynamics had an impact on sarcomere structure. To visualize sarcomere dynamics at the cellular scale, we infected the iPSC-CMs with lentiviral constructs containing both fluorescently labeled α–actinin-2 and N-cadherin and observed their dynamics in monolayer cultures of iPSC-CMs under time-lapse microscopy. The previously observed fast remodeling of N-cadherin junction in *PKP2*tv monolayers was accompanied by constant dissociation and reformation of the sarcomere network (Fig. 9, A and B, and movies S9 to S12). When we used the same optical tracking method to quantify sarcomeric (α–actinin-2) motion in these movies (movies S9 to S12), we found a significant increase in the net displacement of sarcomeric α–actinin-2 in *PKP2*tv monolayers (Fig. 9C), while the mean displacement per frame is not significantly different from the WT cells (Fig. 9D). Here, the ramble motion of α–actinin-2 is significantly lower in *PKP2*tv monolayers (Fig. 9E), indicating that the sarcomeric α–actinin-2 movement is more directional and marked compared to the WT cells. Together, these results suggest that sarcomere stability in multicellular cardiac syncytia is impaired by *PKP2*tvs.

We further hypothesized that this sarcomere instability affects the overall sarcomere content in multicellular structures, ultimately resulting in compromised force generation. To test this hypothesis, we immunostained for α–actinin-2 in multicellular cardiac patches adherent to ECM islands and quantified the total number of α–actinin-2 containing sarcomere *z*-discs (Fig. 10A). We found a significantly lower number of sarcomeres in cardiac patches harboring *PKP2*tvs as compared to WT controls (Fig. 10B), which is consistent with their impaired systolic force generation (Fig. 6, C to E). Conversely, the total number of sarcomeres was significantly higher in single cells harboring *PKP2*tv$^{+/-}$ compared to WT1 (fig. S3, A and B), which also corresponds to their increased systolic force generation (Fig. 5, C to E). Furthermore, in addition to affecting sarcomere content, we examined whether PKP2tvs disrupted sarcomere organization. We evaluated the order parameter (O.P.) for sarcomere alignment, which measures how consistently all sarcomeres are oriented at a certain radial distance from any sarcomere of interest; an O.P. of 1 indicates perfect alignment in that all other sarcomeres are parallel to the sarcomere of interest (Fig. 10C). We found that the sarcomere alignment drops to a lower level in cardiac patches harboring *PKP2*tvs when evaluating the alignment at 50-μm distance (Fig. 10D) or at a longer distance by model prediction (Fig. 10E), indicating decreased order in sarcomere alignment in multicellular cardiac syncytia harboring *PKP2*tvs. Notably, the sarcomere alignment in micropatterned single cells is maintained at a similarly high level in *PKP2*tv$^{+/-}$ compared to WT1 (fig. S3, C to E). Together, these results reveal that *PKP2*tvs, through their effects on destabilizing cell-cell junctions, destabilize sarcomere networks and result in a reduced sarcomere content and alignment in multicellular cardiac syncytia.

DISCUSSION

ACM modeling using animals, primary cells, and iPSCs has revealed mechanisms by which pathogenic variants in desmosomal genes lead to arrhythmias and fibrofatty deposition (*51*). However, the

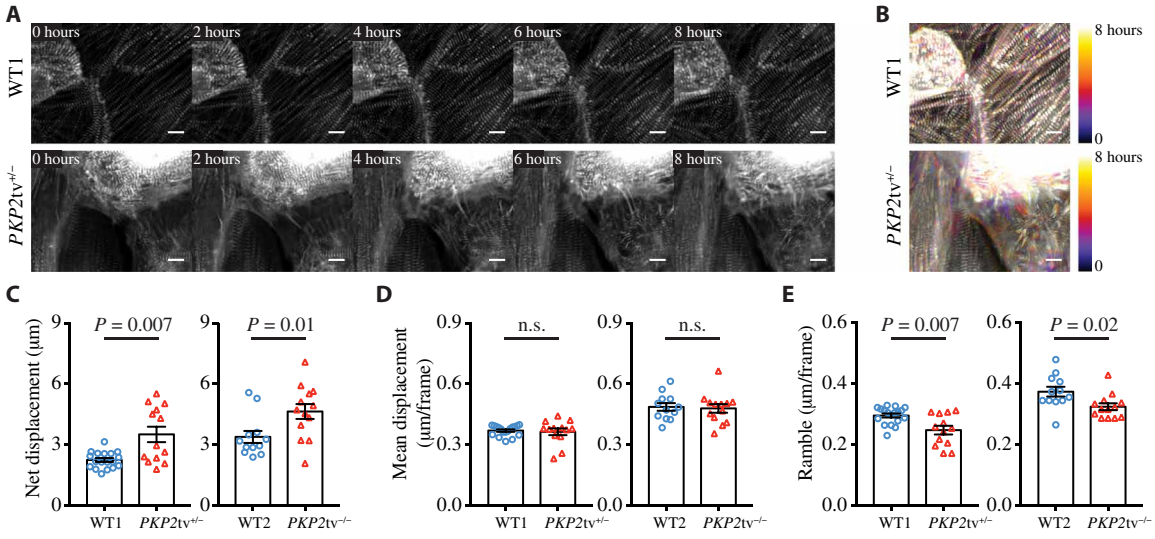

Fig. 9. *PKP2*tvs destabilize sarcomeres. (**A**) Representative time-lapse images of sarcomeric α–actinin-2 at 0, 2, 4, 6, and 8 hours into the live imaging of monolayer cultures of iPSC-CMs comparing *PKP2*tv$^{+/-}$ versus WT1. Scale bars, 10 μm. (**B**) Temporal color-coded hyperstacks of representative sarcomeric α–actinin-2 time-lapse movies showing stable sarcomere structures in in monolayer cultures of WT1 and unstable sarcomeres in *PKP2*tv$^{+/-}$. Scale bars, 10 μm. (**C**) Net displacement of sarcomeric α–actinin-2 in time-lapse movies measured by optical flow tracking shows a significant increase in monolayer cultures of *PKP2*tv$^{+/-}$ ($n = 13$) versus WT1 ($n = 18$) and in *PKP2*tv$^{-/-}$ ($n = 13$) versus WT2 ($n = 12$). (**D**) Mean displacement per frame of junctional N-cadherin in time-lapse movies measured by optical flow tracking shows comparable mean displacement per frame in monolayer cultures of *PKP2*tv$^{+/-}$ ($n = 13$) versus WT1 ($n = 18$) and in *PKP2*tv$^{-/-}$ ($n = 13$) versus WT2 ($n = 12$). (**E**) Ramble of junctional N-cadherin in time-lapse movies measured by optical flow tracking shows a significant decrease in monolayer cultures of *PKP2*tv$^{+/-}$ ($n = 13$) versus WT1 ($n = 18$) and in *PKP2*tv$^{-/-}$ ($n = 13$) versus WT2 ($n = 12$). Statistics: Individual data points across three independent experiments are shown with means ± SEM on plots; Student's *t* test, $\alpha = 0.05$.

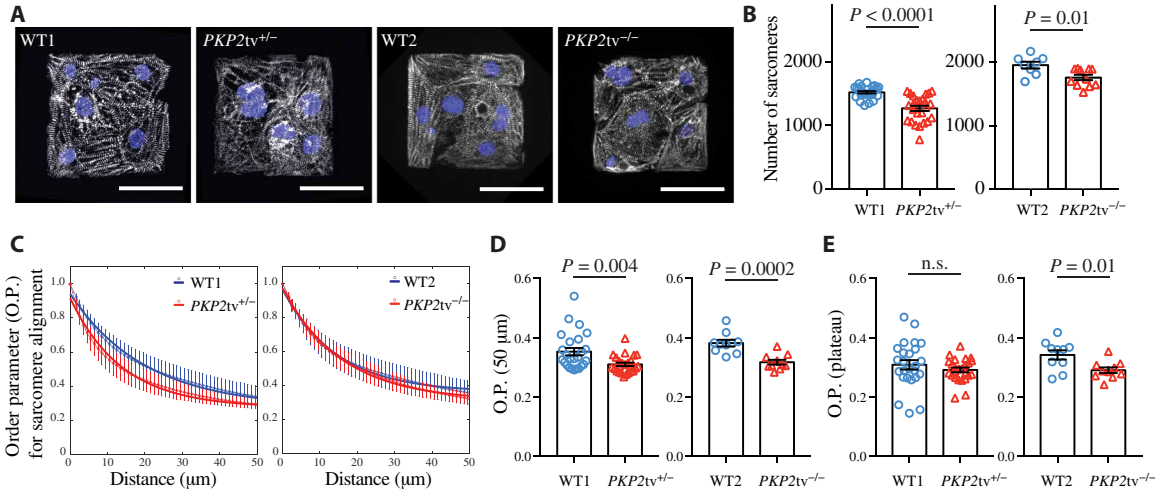

Fig. 10. *PKP2*tvs impair sarcomere content and organization in multicellular cardiac patches. (**A**) Representative images of cardiac patches immunostained for sarcomeric α–actinin-2 (gray) and nuclei (blue). Scale bars, 50 μm. (**B**) Quantification of the number of α–actinin-2–positive sarcomeric *z*-discs in each cardiac patch shows significantly less sarcomere content in *PKP2*tv$^{+/-}$ ($n = 25$) versus WT1 ($n = 25$) and in *PKP2*tv$^{-/-}$ ($n = 11$) versus WT2 ($n = 8$). (**C**) Order parameter (O.P.) for sarcomere alignment plotted over distance from any sarcomere *z*-disc comparing cardiac patches formed with *PKP2*tv$^{+/-}$ ($n = 25$) versus WT1 ($n = 25$) and *PKP2*tv$^{-/-}$ ($n = 1$) versus WT2 ($n = 8$). Data are shown as means (dots) ± SD (bars) with the solid lines showing data fitted in an exponential decay model. (**D**) Quantification of O.P. at 50 μm away from any sarcomere *z*-disc shows a significant decrease in sarcomere alignment in cardiac patches formed with *PKP2*tv$^{+/-}$ ($n = 25$) versus WT1 ($n = 25$) and in *PKP2*tv$^{-/-}$ ($n = 11$) versus WT2 ($n = 8$). (**E**) Quantification of the plateau of O.P. decay model shows comparable levels of sarcomere alignment in long range in cardiac patches formed with *PKP2*tv$^{+/-}$ ($n = 25$) versus WT1 ($n = 25$) and significantly lower levels of sarcomere alignment in *PKP2*tv$^{-/-}$ ($n = 11$) versus WT2 ($n = 8$). Statistics: Individual data points across three independent experiments are shown with means ± SEM on plots, unless otherwise specified; Student's *t* test, $\alpha = 0.05$. Immunostains are representative of at least three independent experiments.

mechanisms leading to loss of cardiac systolic function are still poorly defined. In this study, we find that *PKP2*tvs can directly compromise multicellular cardiac contractility by destabilizing sarcomere organization. How PKP2 loss might drive these effects could be through multiple mechanisms. *PKP2* mutations have been shown to alter the Hippo-YAP signaling pathway, which is known to be critical for driving transcriptional programs that regulate cytoskeletal maturation (*15*). Loss of PKP2 in nonmyocytes has also

been shown to modulate RhoA activity and localization, leading to cortical regulation of cytoskeletal reorganization (*52*). In addition to transcriptional and biochemical signaling mechanisms previously described (*9*–*11*, *15*, *52*), the direct impact of PKP2 on junctional stability highlighted in this study could alter sarcomere stability via a mechanical pathway. PKP2 is not only a scaffolding protein that is critical for the assembly of desmosome complexes (*53*) but can also bind to N-cadherin via αT-catenin (*54*, *55*), hence establishing a close association between desmosomes and adherens junctions to form a hybrid junction area composita that mechanically anchors the cytoskeleton of neighboring CMs. Despite the critical roles for N-cadherin in gap junction assembly and electrical conduction (*56*), the intercellular alignment of myofibrils (*57*), and myocardial cell adhesion and systolic function (*58*), its junctional localization in ACM CMs is similar to WT controls (*34*). Here, we extend these findings and show that pathogenic variants in desmosomal genes such as *PKP2*tv also did not affect N-cadherin localization but, instead, impaired the dynamics of N-cadherin turnover at the intercalated disc leading to an effectively reduced pool of N-cadherin available for junction remodeling. This impaired N-cadherin stability likely contributes to a loss of mechanical anchoring and loading of the sarcomeres, which has been shown to markedly destabilize them and cause the reduction in cardiac contractility (*59*). To be noted, mutations in the N-cadherin–encoding gene *CDH2* have recently been identified in patients with ACM (*60*).

The cross-talk between PKP2 and N-cadherin could be mediated by other molecules. One potential candidate is the PKP2 binding partner, αT-catenin. It has been shown that PKP2 is reduced in the area composita in αT-catenin–knockout mouse model (*55*). However, we found that αT-catenin expression is not changed in the *PKP2*tv CMs (fig. S4). Another candidate could be plakoglobin (PG), which interacts with both classical cadherins and desmosomal cadherins in the area composita. Reduced PG expression at the intercalated disc was reported in patients with ACM carrying mutations in various desmosomal genes including *PKP2* (*61*). PG reduction was not detected in PKP2-heterozygous-null murine hearts unless the animals were exposed to exercise training (*6*, *10*). Further studies will be required to explore the molecular mechanism for how *PKP2*tvs lead to N-cadherin instability at cell-cell contacts.

Our results suggest that *PKP2*tvs cause a reduction in contractile forces and sarcomere content only in multicellular contexts (Figs. 4, C and D; 6, C to E; and 10, A and B). In contrast, single CMs harboring *PKP2*tvs exhibited increased contractile forces and sarcomere content (Fig. 5, C to E, and fig. S3, A and B). How *PKP2*tv increases contractility in single cells is unclear and could be through multiple mechanisms. Knockdown of *PKP2* in cultured nonmyocytes has been shown to increase RhoA activity, leading to elevated contractile actomyosin activity, increased stress fibers, and larger and more stable focal adhesions (*52*, *62*), all of which could possibly contribute to a higher cellular tension and cytoskeleton reorganization. In addition, in vivo studies identified increased formation of RyR2 super clusters and elevated cytosolic calcium transients in cardiac-specific *PKP2* knockout mice (*11*), which could readily enhance contractility of single cells, thus inducing force-dependent sarcomere assembly. Nonetheless, our studies suggest that the destabilizing effects of *PKP2*tv in the presence of cell-cell adhesions can dominate over these cell autonomous effects, and further studies will be required to elicit a full picture of the complex relationship between calcium handling, sarcomere organization, and contractility during ACM disease progression.

A carefully orchestrated interplay between cell-cell junctions, cell-ECM adhesion, and sarcomere organization may be emerging as a general theme relevant to cardiac development and disease. CMs in early embryonic development are initially round in shape with randomly oriented nascent myofibrils, with cell-ECM and cell-cell adhesion complexes surrounding the whole cell (*63*). As cardiac development progresses, cell-cell and cell-ECM adhesions segregate and become restricted to the narrow ends and lateral membrane of matured CMs respectively as CMs elongate and sarcomeres assemble and align (*63*, *64*). Conversely, many human cardiomyopathies are characterized by lateralization of cell-cell adhesions, increased expression of cell-matrix adhesions, and structural changes to myofibrils and the associated sarcomeres (*65*, *66*). The direct coregulation among cell-cell and cell-matrix adhesions has been described in many contexts, and PKP2 deficiency has been reported to strengthen cell-ECM adhesions highlighting such cross-talk between the two types of adhesions (*62*). Recent studies have also demonstrated a role for cell-ECM adhesions in driving sarcomere assembly (*59*). Here, our findings linking instability in cell-cell junctions and disruption of sarcomere organization add to this work and further underscore the need to better understand these interactions to gain broader insights into disease pathogenesis.

In the pathogenesis of HCM or DCM, aberrant cardiac contractility arising from sarcomeric dysfunction is a well-established concept. For instance, some DCM-causing mutations are found to disrupt sarcomere formation, and the reduced sarcomere content in turn leads to decreased cardiac contractility (*59*). In the current study, the demonstration that a genetic mutation associated with ACM can also disrupt sarcomeres and CM force generation would suggest a potentially closer link between ACM and DCM. Although ACM is classically considered a distinct disease from DCM, similarities between their clinical phenotypes have begun to emerge. ACM was historically considered a right ventricular only/dominant disease but is now being recognized as a disease that could also present with left ventricular involvement and clinical features of DCM including ventricular dilation and systolic dysfunction (*30*). Conversely, 30 to 40% of patients with DCM present with ventricular arrhythmias (*67*). Last, with advances in genetic screening, numerous mutations including those in *TTN*, *DES*, *LMNA*, and even *PKP2* have been identified in patients clinically described as ACM or DCM (*3*, *68*, *69*). This study is the first to demonstrate a direct impact of ACM-causing *PKP2* mutations on cardiac contractility and sarcomere organization, and our data reveal fundamental pathogenic mechanisms that may be shared among different types of cardiomyopathies and suggest that it may be possible to adapt clinical management and treatment strategies from other better studied disease such as DCM in treating ACM.

MATERIALS AND METHODS

Generation of human iPSCs with *PKP2*tvs

Two human iPSC lines from different donors, WTC (AICS-0017, Allen Institute) and PGP1 (Personal Genome Project), were used to generate the lines in the current study. *PKP2*tv$^{+/-}$ and its control (WT1) were generated from the WTC iPSCs and *PKP2*tv$^{-/-}$ and its control (WT2) from PGP1 iPSCs. Truncating mutations were introduced to the *PKP2* gene in these WT iPSCs using CRISPR-Cas9–mediated genome editing technology as previously described (*70*). Briefly, the pCR-Blunt II-TOPO vector (K280002, Thermo

Fisher Scientific) cloned with CRISPR guide RNAs targeting *PKP2* exon2, and the Cas9 vector pSpCas9(BB)-2A-Puro (PX459) V2.0 (Addgene plasmid #62988) were transfected into the WT iPSCs via nucleofection. Following the electroporation process, iPSCs that successfully took up the Cas9-Puro plasmid were selected using puromycin treatment and were subsequently replated for monoclonal expansion and genetic validation via MiSeq sequencing (Illumina). This monoclonal expansion process was repeated twice sequentially to ensure that the iPSC colonies of interests were homogenously composed of genotypically identical cells. Isogenic iPSCs with WT or *PKP2*tvs were maintained in complete mTeSR1 medium (STEMCELL Technologies) on Matrigel-coated (Corning) plates.

iPSC differentiation and CM maintenance

iPSCs were differentiated into CMs as described previously (*71*). Specifically, iPSCs were differentiated in RPMI 1640 medium (Thermo Fisher Scientific) supplemented with B27 minus insulin (Thermo Fisher Scientific) by sequential targeting of the WNT pathway—activating the WNT pathway using 8 to 12 μM of CHIR99021 (Tocris) on day 0 for 24 hours and inhibiting the WNT pathway using 5 μM of IWP4 (Tocris) on day 3 for 48 hours. CMs were isolated after showing spontaneous beating (between day 9 and day 14) using metabolic selection by adding 4 mM of DL-lactate (Sigma-Aldrich) in glucose free RPMI 1640 medium (Thermo Fisher Scientific) for 4 days. Following selection, CMs were passaged onto six-well plates coated with fibronectin (10 μg/ml; Corning), maintained in RPMI 1640 medium supplemented with B27 (Thermo Fisher Scientific), and used for assays 2 weeks after passaging around day 30 after initiation of differentiation.

Antibodies, immunofluorescence, and Western blotting

Anti–α–actinin-2 was from Abcam [ab9465 (1:500) and ab137346 (1:200)] and Fitzgerald (70R-1068; 1:200). Anti-PKP2 was from SLBio (LS-C85371; 1:200). Anti-desmoplakin was from Abcam (ab71690; 1:200). Anti-Cx43 was from Abcam (ab11370; 1:200). Anti–N-cadherin was from Cell Signaling Technology (#14215; 1:100).

CMs cultured in growth medium were perm/fixed with 0.03% Triton X-100 (Thermo Fisher Scientific) and 1% paraformaldehyde (Thermo Fisher Scientific) in phosphate-buffered saline (PBS) containing calcium and magnesium (PBS^+) at 37°C for 90 s. Cells were immediately postfixed in 4% paraformaldehyde in PBS^+ at 37°C for 15 min. Cells were rinsed three times with PBS^+ and permeabilized with 0.5% Triton X-100 in PBS^+ for 10 min. Cells were blocked with 2% bovine serum albumin (BSA; Sigma-Aldrich) in PBS^+. Primary and secondary antibodies were applied in 2% BSA in PBS^+ and rinsed three times over 30 min with PBS^+ between each treatment. For Western blot analyses, CMs were lysed in 2× NuPAGE LDS Sample Buffer (Life Technologies) containing 100 mM dithiothreitol and analyzed by SDS–polyacrylamide gel electrophoresis and immunoblotting with chemiluminescent horseradish peroxidase detection. Immunofluorescent images and Western blots were adjusted for brightness and contrast using ImageJ software (National Institutes of Health, Bethesda, MD).

Immunofluorescence quantification

To quantify fluorescence intensities of junctional desmoplakin and Cx43, grayscale images of cells immunostained for N-cadherin were converted to a binary mask to define the junction areas, and the average intensity of immunofluorescence from desmoplakin or Cx43 within the masked junction areas was calculated for each sample.

Quantitative polymerase chain reaction

Cells were lysed with TRIzol (Life Technologies), followed by chloroform phase separation. The aqueous phase was diluted with 70% ethanol at 1:1 ratio, loaded on a RNA micro column (RNA Micro Kit, QIAGEN Sciences) and RNA extraction proceeded according to the manufacturer's protocol. Subsequently, 0.5 μg of total RNA was converted to complementary DNA (cDNA) with qScript cDNA Supermix (Quanta Sciences). Real-time polymerase chain reaction (PCR) was performed in 20 μl of reactions using the power SYBR Green Master Mix (Applied Biosciences, Thermo Fisher Scientific) and a QuantStudio3 (Applied Biosciences, Thermo Fisher Scientific), cycling at 95°C for 15 s then 60°C for 60 s for 40 cycles. Specific gene targets were detected with primer set against *PKP2* (GAGAGCGCACTTGACTGTCG and CTCCATGTCTGCATTCCCCAG) and the housekeeping gene proteasome subunit beta type 2 (PSMB2, ACTATGTTCTTGTCGCCTCCG and CTGTACAGTGTCTCCAGCCTC). Relative gene expression is calculated as $2^{-\Delta\Delta CT} \pm$ SEM, in which ΔCT is equal to the cycle threshold (CT) of the PKP2 minus CT of PSMB2 and ΔΔCT is equal to the ΔCT of any sample minus the average ΔCT of WT repeats. At least three biological replicates (three independent batches of stem cell differentiation) were used. Within each biological replicate, we measured across two samples, and the mean value of these two repeats is shown as a single data point in Fig. 1D.

Action potential measurement

CMs were replated onto fibronectin-coated glass substrates. CAG-FLEX-Archon1-KGC-EGFP-ER2 rAAV2 (Archon1) [multiplicity of infection (MOI), 2000 to 3000] and CMV-Cre AAV9 (Addgene) (MOI, 4000 to 6000) were added 24 hours after replating. Viruses were washed out 2 days later, and CMs were maintained in RPMI 1640 medium supplemented with B27 medium. Imaging was performed 7 days after transduction.

Optical voltage recordings were taken using a one-photon wide-field fluorescence microscope using a PCO Edge 4.2 CLHS sCMOS camera, a 0.95 numerical aperture (NA) 20× water immersion objective (Olympus). The far-red fluorescence was imaged using a NECSEL Red 6.3X, fiber-coupled laser which operates up to 6 W, FF662-FDi01 (Semrock) dichroic filter, and both FF01-635/18 and FF01-736/128 band-pass filters (Semrock). All recordings were acquired at 100 Hz. Samples were maintained at 37°C and 5% CO_2 throughout imaging. Samples were paced with carbon electrodes made from carbon rods (Ladd Research) attached to platinum wires (Sigma-Aldrich) using the C-Pace EM (Ionoptix) at 1.0 Hz with 10 to 20 V with a 10-ms duration.

Cardiac microtissues

Polydimethylsiloxane (PDMS) microtissue devices with tissue wells each containing two cylindrical micropillars with spherical caps were casted from a 3D printed mold (Protolabs). One day before tissue seeding, devices were plasma-treated for 60 s, treated with 0.01% poly-L-lysine (ScienCell) for 2 hours, 0.1% glutaraldehyde (EMS) for 15 min, washed three times with deionized (DI) water, and let sit in DI water at 4°C overnight. Immediately before seeding, devices were soaked in 70% ethanol for 30 min, dried, and sterilized under ultraviolet (UV) for 15 min. After sterilization, 3 μl of 5% BSA was

added to the bottom of each tissue well, and devices were spun in a tabletop centrifuge at 3000 rpm for 1.5 min to evenly distribute the BSA. After 1-hour incubation at room temperature, BSA was removed, and 2 μl of 2% Pluronic F-127 (Sigma-Aldrich) was added to each well and incubated for 30 min at room temperature to prevent CMTs sticking to the bottom surface of the devices.

A total of 60,000 cells per tissue, consisting of 90% iPSC-CMs and 10% human mesenchymal stem cells, were mixed in 7.5 μl of an ECM solution, consisting of human fibrinogen (4 mg/ml; Sigma-Aldrich), 10% Matrigel (Corning), and 0.4 U of thrombin (Sigma-Aldrich) per mg of fibrinogen, 5 μM Y-27632 (Tocris), and aprotinin (0.033 mg/ml; Sigma-Aldrich). The cell-ECM mixture was pipetted into each tissue well, and after gel polymerization for 5 min, tissue maintenance growth medium containing high-glucose Dulbecco's modified Eagle's medium (Thermo Fisher Scientific) supplemented with 10% fetal bovine serum (Sigma-Aldrich), 1% penicillin-streptomycin (Thermo Fisher Scientific), 1% nonessential amino acids (Thermo Fisher Scientific), 1% GlutaMAX (Thermo Fisher Scientific), 5 μM Y-27632, and aprotinin (0.033 mg/ml) were added. The growth medium was replaced every other day. Y-27632 was removed 2 days following seeding, and the aprotinin concentration was decreased to 0.016 mg/ml after 7 days.

Ten days after seeding, the tissues were electrically stimulated at 1 Hz using the IonOptix C-Pace EP Culture Pacer (IonOptix) with a 10-ms square pulse of 10 to 20 V/cm. Time-lapse videos of the tissue contraction were acquired at 30 frames/s using a 4× objective on a Nikon Eclipse Ti (Nikon Instruments Inc.) with an Evolve EMCCD camera (Photometrics) or on a Zeiss Axiovert 200 M inverted spinning disk microscope with an ORCA-100 camera (Hamamatsu) equipped with a temperature and CO_2-equilibrated environmental chamber. Maximum contractile force, stress, and contraction kinetics were calculated using a custom MATLAB script based on the deflection of the pillars and the measured pillar spring constant of 2.68 μN/μm, as described previously (*41*).

Micropatterned PAA hydrogel

Fibronectin (Corning) was conjugated to acrylic acid *N*-hydroxysuccinimide (acrylic-NHS) (Sigma-Aldrich) at a concentration of fibronectin (0.1 mg/ml) and acrylic-NHS (4 mg/ml) in 1× PBS for 1 hour at room temperature. Following conjugation, the solution was coated on PDMS stamps patterned with arrays of 2000-μm^2 rectangles with a 1:7 aspect ratio or with arrays of 100 μm by 100 μm squares for 1 hour at room temperature. The stamps were rinsed once with water and air-dried before microcontact printing the conjugated fibronectin onto clean glass coverslips to get the micropatterned coverslips for making PAA gels.

PAA gels of 7.9- and 4-kPa stiffness were made by adjusting acrylamide and bisacrylamide stock solution (Bio-Rad Laboratories) concentrations (*50*). A solution of 40% acrylamide, 2% bisacrylamide, and 1× PBS was polymerized by adding tetramethylethylene diamine (Fisher BioReagents) and 1% ammonium persulfate. A droplet of the gel solution supplemented with 0.2- or 0.5-μm fluorescent beads solution (Bangs Laboratories Inc.) was deposited on a glass-bottom dish (MatTek) that was plasma-activated for 1 min and treated with a solution of 2% (v/v) 3-(trimethoxysilyl)propyl methacrylate (Sigma-Aldrich) and 1% acetic acid in ethanol for 10 min. Micropatterned coverslips were placed fibronectin side down on the gel droplet, allowing the gel solution to incorporate the acrylic-NHS-fibronectin complex during polymerization. Gels were polymerized for 45 min at room temperature and soaked in 1× PBS before the coverslips were carefully detached from the gel. Gel substrates were washed with 1× PBS, UV-sterilized, and stored in 1× PBS until cell seeding. Immediately before cell seeding, gels were incubated in a fibronectin solution (0.1 mg/ml) at 37°C for 30 min.

Traction force microscopy

TFM measurements were obtained 7 days after cell seeding. Time-lapse images of beads moving near the substrate surface, distributed in and around the contact region of a single cell or cell patch, were acquired at 30 frames/s with a Yokogawa CSU-21/Zeiss Axiovert 200 M inverted spinning disc microscope with a Zeiss LD C-Apochromat 40×, 1.1 NA water-immersion objective or a Zeiss 25×, oil-immersion objective, and an ORCA-100 camera (Hamamatsu), while the cells were electrically stimulated to beat at 1 Hz on the microscope stage equipped with a temperature and CO_2-equilibrated environmental chamber.

The traction forces exerted by iPSC-CMs on the gel substrates were computed by measuring the displacement of fluorescent beads embedded within the gel with reference to the beads' positions at peak relaxation, as described previously (*72*) (software available at https://sites.google.com/site/qingzongtseng/tfm). The traction stress vector fields were generated using an open source package of Fiji plugins [developed by Tseng *et al.* (*72*)] and were interpolated with a custom MATLAB script. Root mean squares (RMSs) of the magnitudes of stress vectors in a user-defined area were computed using the formula: $S_{RMS} = \sqrt{\frac{1}{n}(|S_1|^2 + |S_2|^2 + \ldots + |S_n|^2)}$, in which S_n is a single stress vector. The work generated by cell contraction was calculated by multiplying force vectors by bead displacement vectors and summing over a user-defined area. Magnitudes of RMS stress and work over time for each video were smoothed, and peak magnitudes at systole were identified and averaged more than three or four beats.

Recombinant cloning and lentiviral transduction

Human N-cadherin (#18870, Addgene) and α–actinin-2 (#52669, Addgene) were PCR-amplified and cloned with C-terminal EGFP-tag or mApple-tag and N-terminal mApple-tag or EGFP-tag, respectively, into a modified pRRL lentiviral expression vector. The pRRL plasmids containing N-cadherin–EGFP and mApple–α–actinin-2 (or N-cadherin–mApple and EGFP–α–actinin-2) were cotransfected with pVSVG, pRSV-REV, and pMDLg/pRRE packaging plasmids into human embryonic kidney–293T cells using calcium phosphate transfection. After 48 hours, viral supernatants were collected, concentrated using PEG-it viral precipitator (SBI), and resuspended in PBS. CMs were transduced in growth medium overnight, and medium was replaced the following morning.

Glass substrates for imaging

Glass substrates for imaging were prepared as described previously (*59*). Briefly, glass substrates were spin-coated with PDMS and polymerized in a 60°C oven overnight. For monolayer culture, PDMS-coated glass substrates were incubated with fibronectin (10 μg/ml) for 1 hour at 37°C before cell seeding. Alternatively, micropatterned PDMS-coated substrates were used to culture cardiac cell patches. PDMS stamps were coated with fibronectin (100 μg/ml) for 1 hour at room temperature and stamped onto PDMS-coated glass substrates that were preactivated in a UV Ozone cleaner (JetLight) for 7 min. Patterned substrates were treated with 0.2%

Pluronic F-127 (Sigma-Aldrich) for 1 hour before cell seeding to prevent nonspecific adhesion of cells to the unpatterned areas of the substrate.

Fluorescence recovery from photobleaching

iPSC-CMs expressing N-cadherin–EGFP or N-cadherin–mApple via lentiviral infection were cultured on micropatterned substrates for 7 days before FRAP measurements. Images of regions of interests (ROIs) of a user-defined size, controlled across samples and experiments, were taken before and after photobleaching of selected ROIs by a 488-nm laser at full power for 1 min and were acquired with a Leica HCX APO L U-V-1 40×/0.80 WATER on an upright Leica TCS SP8 multiphoton microscope equipped with a temperature and CO_2-equilibrated environmental chamber. Postphotobleaching images were acquired every 30 s for 30 min. To calculate the percentage recovery of N-cadherin, the fluorescence intensity of N-cadherin in each photobleached ROI was background-subtracted, normalized to an unbleached reference region, and divided by the intensity in the ROI before photobleaching.

Time-lapse fluorescence microscopy

iPSC-CMs expressing N-cadherin–EGFP and mApple–α–actinin-2 (or N-cadherin–mApple and EGFP–α–actinin-2) via lentiviral infection were cultured on glass substrates for 7 days before live imaging of the N-cadherin and α–actinin-2 dynamics. During the time-lapse imaging, iPSC-CMs were maintained in growth medium containing OxyFluo (Oxyrase) in a temperature and CO_2-equilibrated environmental microscope chamber and imaged every 10 min overnight on a Nikon Ti Eclipse epifluorescence microscope with a Nixon Plan Fluor 40×, 1.3 NA objective and an Evolve EMCCD camera (Photometrics).

Motion tracking using optical flow

A custom Python script with user input is used to analyze the dynamics of N-cadherin at the cell-cell junctions. A time-lapse movie of N-cadherin fluorescence that spans 8 hours is used as an input. First, the optical flow between all adjacent frames in the entire image stack is calculated using a dense, image patch–based, two-frame motion estimation method (Farnebäck algorithm; OpenCV). Large displacements between adjacent frames are robustly captured because of its multiscale nature. We typically use a five-level image pyramid decomposition with a scale of 0.5. An image patch size of 9 was chosen to avoid spatial blurring of the computed optical flow without compromising our ability to record large movements. Likewise, we used a polynomial expansion neighborhood of size 7, and the SD of the Gaussian smoothing function was 1.5 in our calculations. The resulting optical flow stack (of size N-1) consists of 2D displacement vectors for each pixel between adjacent frames. Using this stack of displacement vectors, each pixel at any given frame can be mapped back to its original location on the first frame at the start of the time lapse (or vice versa). We calculated three maps for each time lapse using the stack of displacement vectors (with spatially consistent mapping) (fig. S2): (i) a map of the final displacement of each point from the first frame and the last frame, i.e., total translation, calculated using a vector sum; (ii) the scalar average of displacements per frame of each point mapped onto the locations in the starting frame; and (iii) a random motion (ramble) map that captures movements at the junction that did not result in net translation; a sum of the scalar displacements minus the translation displacement. Cell-cell contacts are then obtained from a user interface that allows the selection of multiple polylines on the first frame, which denote the boundaries between cells. This set of polylines (increased to a width of 10 pixels) was then used as a mask on top of the three maps described above. The mean value of these three maps based on the mask denotes the net displacement, mean displacement per frame, and ramble motion per frame. The same methods were also used for characterizing the dynamics of α–actinin-2 by changing the user selection from multiple polylines to multiple polygons that denote the regions with α–actinin-2 signal.

Quantification of O.P. for sarcomere alignment

A custom MATLAB script was used to quantify the sarcomere periodicity and order from α–actinin-2–labeled images. Our approach is based on first detecting all the *z*-discs in the image and identifying the local alignment of sarcomere filament to then subsequently extract the overall sarcomere periodicity and order. The *z*-discs were identified by first preprocessing the image with a morphological top-hat filter and using an adaptive thresholding algorithm. The resulting *z*-disc binary mask was used to extract the centroids of all sarcomeres in the image. A small image patch around each *z*-disc was used to perform image autocorrelation in the neighborhood to determine the local orientation of the sarcomere at each *z*-disc. The direction of maximum periodicity at each *z*-disc was identified from the location of peaks in the autocorrelation image in the spatial interval of 1.6 to 2.2 μm. Knowing the location of each *z*-disc and the local orientation of the sarcomeres, we then identified the neighboring sarcomeres and constructed an empirical probability distribution function from these set of points. The decay length (λ) was calculated from an exponential fit ($a_0 + a_1 e^{-x/\lambda}$) of the peaks in the probability distribution function. We computed the orientational order of all the *z*-discs in the image using the function $\langle \tfrac{3}{2}\cos^2\theta - \tfrac{1}{2} \rangle$, where θ is the angular offset between each sarcomere and a fixed global vector $\hat{n}$ of maximal order (director). In addition, we calculated the persistence of order by measuring the drop in this computed O.P. as the neighborhood radius around each *z*-disc is increased (with the orientation of the central *z*-disc for each neighborhood as the director $\hat{n}$).

Statistical analysis

Sample sizes and *P* values are reported in each figure. Two-tailed, unpaired Student's *t* tests assuming unequal variances, significance level $\alpha = 0.05$, comparing isogenic pairs of cell lines (WT1 versus *PKP2*tv$^{+/-}$; and WT2 versus *PKP2*tv$^{-/-}$), were performed using GraphPad Prism 7.5. In the figures, unless otherwise noted, graphs show means ± SEM.

SUPPLEMENTARY MATERIALS

Supplementary material for this article is available at https://science.org/doi/10.1126/sciadv.abh3995

View/request a protocol for this paper from *Bio-protocol*.

REFERENCES AND NOTES

1. D. Corrado, C. Basso, D. P. Judge, Arrhythmogenic cardiomyopathy. *Circ. Res.* **121**, 784–802 (2017).
2. A. Asimaki, A. G. Kleber, J. E. Saffitz, Pathogenesis of arrhythmogenic cardiomyopathy. *Can. J. Cardiol.* **31**, 1313–1324 (2015).
3. E. T. Hoorntje, W. P. Te Rijdt, C. A. James, K. Pilichou, C. Basso, D. P. Judge, C. R. Bezzina, J. P. van Tintelen, Arrhythmogenic cardiomyopathy: Pathology, genetics, and concepts in pathogenesis. *Cardiovasc. Res.* **113**, 1521–1531 (2017).

4. E. McNally, H. MacLeod, L. Dellefave-Castillo, Arrhythmogenic right ventricular cardiomyopathy, in *GeneReviews [Internet]* (University of Washington, 2017).
5. E. M. Oxford, H. Musa, K. Maass, W. Coombs, S. M. Taffet, M. Delmar, Connexin43 remodeling caused by inhibition of plakophilin-2 expression in cardiac cells. *Circ. Res.* **101**, 703–711 (2007).
6. M. Cerrone, M. Noorman, X. Lin, H. Chkourko, F. X. Liang, R. van der Nagel, T. Hund, W. Birchmeier, P. Mohler, T. A. van Veen, H. V. van Rijen, M. Delmar, Sodium current deficit and arrhythmogenesis in a murine model of plakophilin-2 haploinsufficiency. *Cardiovasc. Res.* **95**, 460–468 (2012).
7. M. Cerrone, M. Delmar, Desmosomes and the sodium channel complex: Implications for arrhythmogenic cardiomyopathy and brugada syndrome. *Trends Cardiovasc. Med.* **24**, 184–190 (2014).
8. P. Y. Sato, H. Musa, W. Coombs, G. Guerrero-Serna, G. A. Patino, S. M. Taffet, L. L. Isom, M. Delmar, Loss of plakophilin-2 expression leads to decreased sodium current and slower conduction velocity in cultured cardiac myocytes. *Circ. Res.* **105**, 523–526 (2009).
9. M. Cerrone, J. Montnach, X. Lin, Y. T. Zhao, M. Zhang, E. Agullo-Pascual, A. Leo-Macias, F. J. Alvarado, I. Dolgalev, T. V. Karathanos, K. Malkani, C. J. M. Van Opbergen, J. J. A. van Bavel, H. Q. Yang, C. Vasquez, D. Tester, S. Fowler, F. Liang, E. Rothenberg, A. Heguy, G. E. Morley, W. A. Coetzee, N. A. Trayanova, M. J. Ackerman, T. A. B. van Veen, H. H. Valdivia, M. Delmar, Plakophilin-2 is required for transcription of genes that control calcium cycling and cardiac rhythm. *Nat. Commun.* **8**, 106 (2017).
10. C. J. van Opbergen, M. Noorman, A. Pfenniger, J. S. Copier, S. H. Vermij, Z. Li, R. van der Nagel, M. Zhang, J. M. de Bakker, A. M. Glass, P. J. Mohler, S. M. Taffet, M. A. Vos, H. V. van Rijen, M. Delmar, T. A. van Veen, Plakophilin-2 haploinsufficiency causes calcium handling deficits and modulates the cardiac response towards stress. *Int. J. Mol. Sci.* **20**, 4076 (2019).
11. J. C. Kim, M. Perez-Hernandez, F. J. Alvarado, S. R. Maurya, J. Montnach, Y. Yin, M. Zhang, X. Lin, C. Vasquez, A. Heguy, F. X. Liang, S. H. Woo, G. E. Morley, E. Rothenberg, A. Lundby, H. H. Valdivia, M. Cerrone, M. Delmar, Disruption of Ca2+iHomeostasis and connexin 43 hemichannel function in the right ventricle precedes overt arrhythmogenic cardiomyopathy in plakophilin-2-deficient Mice. *Circulation* **140**, 1015–1030 (2019).
12. J. Moncayo-Arlandi, E. Guasch, M. Sanz-de la Garza, M. Casado, N. A. Garcia, L. Mont, M. Sitges, R. Knoll, B. Buyandelger, O. Campuzano, A. Diez-Juan, R. Brugada, Molecular disturbance underlies to arrhythmogenic cardiomyopathy induced by transgene content, age and exercise in a truncated PKP2 mouse model. *Hum. Mol. Genet.* **25**, 3676–3688 (2016).
13. A. Lorenzon, M. Calore, G. Poloni, L. J. De Windt, P. Braghetta, A. Rampazzo, Wnt/β-catenin pathway in arrhythmogenic cardiomyopathy. *Oncotarget* **8**, 60640–60655 (2017).
14. A. A. Khudiakov, D. A. Kostina, A. A. Kostareva, A. N. Tomilin, A. B. Malashicheva, The effect of plakophilin-2 gene mutations on activity of the canonical Wnt signaling pathway. *Tsitologiia* **57**, 868–875 (2015).
15. S. N. Chen, P. Gurha, R. Lombardi, A. Ruggiero, J. T. Willerson, A. J. Marian, The hippo pathway is activated and is a causal mechanism for adipogenesis in arrhythmogenic cardiomyopathy. *Circ. Res.* **114**, 454–468 (2014).
16. A. D. Dubash, C. Y. Kam, B. A. Aguado, D. M. Patel, M. Delmar, L. D. Shea, K. J. Green, Plakophilin-2 loss promotes TGF-β1/p38 MAPK-dependent fibrotic gene expression in cardiomyocytes. *J. Cell Biol.* **212**, 425–438 (2016).
17. S. H. Vermij, H. Abriel, T. A. van Veen, Refining the molecular organization of the cardiac intercalated disc. *Cardiovasc. Res.* **113**, 259–275 (2017).
18. L. Puzzi, D. Borin, P. Gurha, R. Lombardi, V. Martinelli, M. Weiss, L. Andolfi, M. Lazzarino, L. Mestroni, A. J. Marian, O. Sbaizero, Knock down of plakophillin 2 dysregulates adhesion pathway through upregulation of miR200b and alters the mechanical properties in cardiac cells. *Cell* **8**, 1639 (2019).
19. T. Meyer, M. Tiburcy, W.-H. Zimmermann, Cardiac macrotissues-on-a-plate models for phenotypic drug screens. *Adv. Drug Deliv. Rev.* **140**, 93–100 (2019).
20. C. A. Blair, B. L. Pruitt, Mechanobiology assays with applications in cardiomyocyte biology and cardiotoxicity. *Adv. Healthc. Mater.* **9**, 1901656 (2020).
21. A. J. S. Ribeiro, B. D. Guth, M. Engwall, S. Eldridge, C. M. Foley, L. Guo, G. Gintant, J. Koerner, S. T. Parish, J. B. Pierson, M. Brock, K. W. Chaudhary, Y. Kanda, B. Berridge, Considerations for an in vitro, cell-based testing platform for detection of drug-induced inotropic effects in early drug development. Part 2: Designing and fabricating microsystems for assaying cardiac contractility with physiological relevance using hum. *Front. Pharmacol.* **10**, 934 (2019).
22. W. J. Polacheck, C. S. Chen, Measuring cell-generated forces: A guide to the available tools. *Nat. Methods* **13**, 415–423 (2016).
23. X. Carvajal-Vergara, A. Sevilla, S. L. D'Souza, Y. S. Ang, C. Schaniel, D. F. Lee, L. Yang, A. D. Kaplan, E. D. Adler, R. Rozov, Y. Ge, N. Cohen, L. J. Edelmann, B. Chang, A. Waghray, J. Su, S. Pardo, K. D. Lichtenbelt, M. Tartaglia, B. D. Gelb, I. R. Lemischka, Patient-specific induced pluripotent stem-cell-derived models of LEOPARD syndrome. *Nature* **465**, 808–812 (2010).
24. N. Sun, M. Yazawa, J. Liu, L. Han, V. Sanchez-Freire, O. J. Abilez, E. G. Navarrete, S. Hu, L. Wang, A. Lee, A. Pavlovic, S. Lin, R. Chen, R. J. Hajjar, M. P. Snyder, R. E. Dolmetsch, M. J. Butte, E. A. Ashley, M. T. Longaker, R. C. Robbins, J. C. Wu, Patient-specific induced pluripotent stem cells as a model for familial dilated cardiomyopathy. *Sci. Transl. Med.* **4**, 130ra147 (2012).
25. C. Kim, J. Wong, J. Wen, S. Wang, C. Wang, S. Spiering, N. G. Kan, S. Forcales, P. L. Puri, T. C. Leone, J. E. Marine, H. Calkins, D. P. Kelly, D. P. Judge, H.-S. V. Chen, Studying arrhythmogenic right ventricular dysplasia with patient-specific iPSCs. *Nature* **494**, 105–110 (2013).
26. A. Brodehl, H. Ebbinghaus, M. A. Deutsch, J. Gummert, A. Gärtner, S. Ratnavadivel, H. Milting, Human induced pluripotent stem-cell-derived cardiomyocytes as models for genetic cardiomyopathies. *Int. J. Mol. Sci.* **20**, 4381 (2019).
27. M. F. Hoes, N. Bomer, P. van der Meer, Concise review: The current state of human in vitro cardiac disease modeling: A focus on gene editing and tissue engineering. *Stem Cells Transl. Med.* **8**, 66–74 (2019).
28. T. Eschenhagen, L. Carrier, Cardiomyopathy phenotypes in human-induced pluripotent stem cell-derived cardiomyocytes—A systematic review. *Pflugers Arch. - Eur. J. Physiol.* **471**, 755–768 (2019).
29. D. T. Paik, M. Chandy, J. C. Wu, Patient and disease–specific induced pluripotent stem cells for discovery of personalized cardiovascular drugs and therapeutics. *Pharmacol. Rev.* **72**, 320–342 (2020).
30. J. A. Towbin, W. J. McKenna, D. J. Abrams, M. J. Ackerman, H. Calkins, F. C. C. Darrieux, J. P. Daubert, C. de Chillou, E. C. DePasquale, M. Y. Desai, N. A. M. Estes 3rd, W. Hua, J. H. Indik, J. Ingles, C. A. James, R. M. John, D. P. Judge, R. Keegan, A. D. Krahn, M. S. Link, F. I. Marcus, C. J. McLeod, L. Mestroni, S. G. Priori, J. E. Saffitz, S. Sanatani, W. Shimizu, J. P. van Tintelen, A. A. M. Wilde, W. Zareba, 2019 HRS expert consensus statement on evaluation, risk stratification, and management of arrhythmogenic cardiomyopathy. *Heart Rhythm.* **16**, e301–e372 (2019).
31. Y. Wada, S. Ohno, T. Aiba, M. Horie, Unique genetic background and outcome of non-Caucasian Japanese probands with arrhythmogenic right ventricular dysplasia/ cardiomyopathy. *Mol. Genet. Genomic Med.* **5**, 639–651 (2017).
32. M. Alcalde, O. Campuzano, P. Berne, P. García-Pavía, A. Doltra, E. Arbelo, G. Sarquella-Brugada, A. Iglesias, L. Alonso-Pulpon, J. Brugada, R. Brugada, Stop-gain mutations in PKP2 are associated with a later age of onset of arrhythmogenic right ventricular cardiomyopathy. *PLOS ONE* **9**, e100560 (2014).
33. A. T. Headrick, J. A. Rosenfeld, Y. Yang, H. Tunuguntla, H. D. Allen, D. J. Penny, J. J. Kim, A. P. Landstrom, Incidentally identified genetic variants in arrhythmogenic right ventricular cardiomyopathy-associated genes among children undergoing exome sequencing reflect healthy population variation. *Mol. Genet. Genomic Med.* **7**, e593 (2019).
34. A. Asimaki, J. E. Saffitz, Remodeling of cell-cell junctions in arrhythmogenic cardiomyopathy. *Cell Commun. Adhes.* **21**, 13–23 (2014).
35. I. El-Battrawy, Z. Zhao, H. Lan, L. Cyganek, C. Tombers, X. Li, F. Buljubasic, S. Lang, M. Tiburcy, W. H. Zimmermann, J. Utikal, T. Wieland, M. Borggrefe, X. B. Zhou, I. Akin, Electrical dysfunctions in human-induced pluripotent stem cell-derived cardiomyocytes from a patient with an arrhythmogenic right ventricular cardiomyopathy. *Europace* **20**, f46–f56 (2018).
36. D. Corrado, A. Zorzi, M. Cerrone, I. Rigato, M. Mongillo, B. Bauce, M. Delmar, Relationship between arrhythmogenic right ventricular cardiomyopathy and brugada syndrome: New insights from molecular biology and clinical implications. *Circ. Arrhythm. Electrophysiol.* **9**, e003631 (2016).
37. K. D. Piatkevich, E. E. Jung, C. Straub, C. Linghu, D. Park, H. J. Suk, D. R. Hochbaum, D. Goodwin, E. Pnevmatikakis, N. Pak, T. Kawashima, C. T. Yang, J. L. Rhoades, O. Shemesh, S. Asano, Y. G. Yoon, L. Freifeld, J. L. Saulnier, C. Riegler, F. Engert, T. Hughes, M. Drobizhev, B. Szabo, M. B. Ahrens, S. W. Flavell, B. L. Sabatini, E. S. Boyden, A robotic multidimensional directed evolution approach applied to fluorescent voltage reporters. *Nat. Chem. Biol.* **14**, 352–360 (2018).
38. S. N. Shroff, S. L. Das, H. A. Tseng, J. Noueihed, F. Fernandez, J. A. White, C. S. Chen, X. Han, Voltage imaging of cardiac cells and tissue using the genetically encoded voltage sensor Archon1. *iScience* **23**, 100974 (2020).
39. G. Tse, Mechanisms of cardiac arrhythmias. *J. Arrhythm.* **32**, 75–81 (2016).
40. J. M. Anumonwo, S. V. Pandit, Ionic mechanisms of arrhythmogenesis. *Trends Cardiovasc. Med.* **25**, 487–496 (2015).
41. W. R. Legant, A. Pathak, M. T. Yang, V. S. Deshpande, R. M. McMeeking, C. S. Chen, Microfabricated tissue gauges to measure and manipulate forces from 3D microtissues. *Proc. Natl. Acad. Sci. U.S.A.* **106**, 10097–10102 (2009).
42. T. Boudou, W. R. Legant, A. Mu, M. A. Borochin, N. Thavandiran, M. Radisic, P. W. Zandstra, J. A. Epstein, K. B. Margulies, C. S. Chen, A microfabricated platform to measure and manipulate the mechanics of engineered cardiac microtissues. *Tissue Eng. Part A* **18**, 910–919 (2012).
43. T. P. Mast, C. A. James, H. Calkins, A. J. Teske, C. Tichnell, B. Murray, P. Loh, S. D. Russell, B. K. Velthuis, D. P. Judge, D. Dooijes, R. J. Tedford, J. F. van der Heijden, H. Tandri,

R. N. Hauer, T. P. Abraham, P. A. Doevendans, A. S. Te Riele, M. J. Cramer, Evaluation of structural progression in arrhythmogenic right ventricular dysplasia/cardiomyopathy. *JAMA Cardiol.* **2**, 293–302 (2017).
44. M. A. Bray, S. P. Sheehy, K. K. Parker, Sarcomere alignment is regulated by myocyte shape. *Cell Motil. Cytoskeleton* **65**, 641–651 (2008).
45. A. J. Ribeiro, Y. S. Ang, J. D. Fu, R. N. Rivas, T. M. Mohamed, G. C. Higgs, D. Srivastava, B. L. Pruitt, Contractility of single cardiomyocytes differentiated from pluripotent stem cells depends on physiological shape and substrate stiffness. *Proc. Natl. Acad. Sci. U.S.A.* **112**, 12705–12710 (2015).
46. W. W. Franke, C. M. Borrmann, C. Grund, S. Pieperhoff, The area composita of adhering junctions connecting heart muscle cells of vertebrates. I. Molecular definition in intercalated disks of cardiomyocytes by immunoelectron microscopy of desmosomal proteins. *Eur. J. Cell Biol.* **85**, 69–82 (2006).
47. C. M. Borrmann, C. Grund, C. Kuhn, I. Hofmann, S. Pieperhoff, W. W. Franke, The area composita of adhering junctions connecting heart muscle cells of vertebrates. II. Colocalizations of desmosomal and fascia adhaerens molecules in the intercalated disk. *Eur. J. Cell Biol.* **85**, 469–485 (2006).
48. J. T. Hinson, A. Chopra, N. Nafissi, W. J. Polacheck, C. C. Benson, S. Swist, J. Gorham, L. Yang, S. Schafer, C. C. Sheng, A. Haghighi, J. Homsy, N. Hubner, G. Church, S. A. Cook, W. A. Linke, C. S. Chen, J. G. Seidman, C. E. Seidman, Heart disease. Titin mutations in iPS cells define sarcomere insufficiency as a cause of dilated cardiomyopathy. *Science* **349**, 982–986 (2015).
49. C. N. Toepfer, A. C. Garfinkel, G. Venturini, H. Wakimoto, G. Repetti, L. Alamo, A. Sharma, R. Agarwal, J. F. Ewoldt, P. Cloonan, J. Letendre, M. Lun, I. Olivotto, S. Colan, E. Ashley, D. Jacoby, M. Michels, C. S. Redwood, H. C. Watkins, S. M. Day, J. F. Staples, R. Padrón, A. Chopra, C. Y. Ho, C. S. Chen, A. C. Pereira, J. G. Seidman, C. E. Seidman, Myosin sequestration regulates sarcomere function, cardiomyocyte energetics, and metabolism, informing the pathogenesis of hypertrophic cardiomyopathy. *Circulation* **141**, 828–842 (2020).
50. A. Chopra, E. Tabdanov, H. Patel, P. A. Janmey, J. Y. Kresh, Cardiac myocyte remodeling mediated by N-cadherin-dependent mechanosensing. *Am. J. Physiol. Heart Circ. Physiol.* **300**, H1252–H1266 (2011).
51. K. M. Austin, M. A. Trembley, S. F. Chandler, S. P. Sanders, J. E. Saffitz, D. J. Abrams, W. T. Pu, Molecular mechanisms of arrhythmogenic cardiomyopathy. *Nat. Rev. Cardiol.* **16**, 519–537 (2019).
52. L. M. Godsel, A. D. Dubash, A. E. Bass-Zubek, E. V. Amargo, J. L. Klessner, R. P. Hobbs, X. Chen, K. J. Green, Plakophilin 2 couples actomyosin remodeling to desmosomal plaque assembly via RhoA. *Mol. Biol. Cell* **21**, 2844–2859 (2010).
53. A. E. Bass-Zubek, R. P. Hobbs, E. V. Amargo, N. J. Garcia, S. N. Hsieh, X. Chen, J. K. Wahl 3rd, M. F. Denning, K. J. Green, Plakophilin 2: A critical scaffold for PKC alpha that regulates intercellular junction assembly. *J. Cell Biol.* **181**, 605–613 (2008).
54. S. Goossens, B. Janssens, S. Bonné, R. De Rycke, F. Braet, J. Van Hengel, F. Van Roy, A unique and specific interaction between αT-catenin and plakophilin-2 in the area composita, the mixed-type junctional structure of cardiac intercalated discs. *J. Cell Sci.* **120**, 2126–2136 (2007).
55. J. Li, S. Goossens, J. Van Hengel, E. Gao, L. Cheng, K. Tyberghein, X. Shang, R. De Rycke, F. Van Roy, G. L. Radice, Loss of αT-catenin alters the hybrid adhering junctions in the heart and leads to dilated cardiomyopathy and ventricular arrhythmia following acute ischemia. *J. Cell Sci.* **125**, 1058–1067 (2012).
56. J. Li, V. V. Patel, I. Kostetskii, Y. Xiong, A. F. Chu, J. T. Jacobson, C. Yu, G. E. Morley, J. D. Molkentin, G. L. Radice, Cardiac-specific loss of N-cadherin leads to alteration in connexins with conduction slowing and arrhythmogenesis. *Circ. Res.* **97**, 474–481 (2005).
57. Y. Luo, G. L. Radice, Cadherin-mediated adhesion is essential for myofibril continuity across the plasma membrane but not for assembly of the contractile apparatus. *J. Cell Sci.* **116**, 1471–1479 (2003).
58. I. Kostetskii, J. Li, Y. Xiong, R. Zhou, V. A. Ferrari, V. V. Patel, J. D. Molkentin, G. L. Radice, Induced deletion of the N-cadheringene in the heart leads to dissolution of the intercalated disc structure. *Circ. Res.* **96**, 346–354 (2005).
59. A. Chopra, M. L. Kutys, K. Zhang, W. J. Polacheck, C. C. Sheng, R. J. Luu, J. Eyckmans, J. T. Hinson, J. G. Seidman, C. E. Seidman, C. S. Chen, Force generation via β-cardiac myosin, titin, and α-actinin drives cardiac sarcomere assembly from cell-matrix adhesions. *Dev. Cell* **44**, 87–96.e85 (2018).
60. B. M. Mayosi, M. Fish, G. Shaboodien, E. Mastantuono, S. Kraus, T. Wieland, M.-C. Kotta, A. Chin, N. Laing, N. B. A. Ntusi, M. Chong, C. Horsfall, S. N. Pimstone, D. Gentilini, G. Parati, T.-M. Strom, T. Meitinger, G. Pare, P. J. Schwartz, L. Crotti, Identification of Cadherin 2 (*CDH2*) mutations in arrhythmogenic right ventricular cardiomyopathy. *Circ. Cardiovasc. Genet.* **10**, e001605 (2017).
61. A. Asimaki, H. Tandri, H. Huang, M. K. Halushka, S. Gautam, C. Basso, G. Thiene, A. Tsatsopoulou, N. Protonotarios, W. J. Mckenna, H. Calkins, J. E. Saffitz, A new diagnostic test for arrhythmogenic right ventricular cardiomyopathy. *N. Engl. J. Med.* **360**, 1075–1084 (2009).
62. J. L. Koetsier, E. V. Amargo, V. Todorović, K. J. Green, L. M. Godsel, Plakophilin 2 affects cell migration by modulating focal adhesion dynamics and integrin protein expression. *J. Invest. Dermatol.* **134**, 112–122 (2014).
63. A. Hirschy, F. Schatzmann, E. Ehler, J. C. Perriard, Establishment of cardiac cytoarchitecture in the developing mouse heart. *Dev. Biol.* **289**, 430–441 (2006).
64. J. C. Wu, H. C. Sung, T. H. Chung, R. M. DePhilip, Role of N-cadherin- and integrin-based costameres in the development of rat cardiomyocytes. *J. Cell. Biochem.* **84**, 717–724 (2002).
65. J. H. Smith, C. R. Green, N. S. Peters, S. Rothery, N. J. Severs, Altered patterns of gap junction distribution in ischemic heart disease. An immunohistochemical study of human myocardium using laser scanning confocal microscopy. *Am. J. Pathol.* **139**, 801–821 (1991).
66. T. Matsushita, M. Oyamada, K. Fujimoto, Y. Yasuda, S. Masuda, Y. Wada, T. Oka, T. Takamatsu, Remodeling of cell-cell and cell-extracellular matrix interactions at the border zone of rat myocardial infarcts. *Circ. Res.* **85**, 1046–1055 (1999).
67. A. Spezzacatene, G. Sinagra, M. Merlo, G. Barbati, S. L. Graw, F. Brun, D. Slavov, A. Di Lenarda, E. E. Salcedo, J. A. Towbin, J. E. Saffitz, F. I. Marcus, W. Zareba, M. R. G. Taylor, L. Mestroni; Familial Cardiomyopathy Registry, Arrhythmogenic phenotype in dilated cardiomyopathy: Natural history and predictors of life-threatening arrhythmias. *J. Am. Heart Assoc.* **4**, e002149 (2015).
68. B. Klauke, A. Gaertner-Rommel, U. Schulz, A. Kassner, E. Z. Knyphausen, T. Laser, D. Kececioglu, L. Paluszkiewicz, U. Blanz, E. Sandica, A. J. van den Bogaerdt, J. P. van Tintelen, J. Gummert, H. Milting, High proportion of genetic cases in patients with advanced cardiomyopathy including a novel homozygous Plakophilin 2-gene mutation. *PLOS ONE* **12**, e0189489 (2017).
69. E. M. McNally, J. R. Golbus, M. J. Puckelwartz, Genetic mutations and mechanisms in dilated cardiomyopathy. *J. Clin. Invest.* **123**, 19–26 (2013).
70. A. Sharma, C. N. Toepfer, T. Ward, L. Wasson, R. Agarwal, D. A. Conner, J. H. Hu, C. E. Seidman, CRISPR/Cas9 mediated fluorescent tagging of endogenous proteins in human pluripotent stem cells. *Curr. Protoc. Hum. Genet.* **96**, 21.11.1–21.11.20 (2018).
71. X. Lian, J. Zhang, S. M. Azarin, K. Zhu, L. B. Hazeltine, X. Bao, C. Hsiao, T. J. Kamp, S. P. Palecek, Directed cardiomyocyte differentiation from human pluripotent stem cells by modulating Wnt/β-catenin signaling under fully defined conditions. *Nat. Protoc.* **8**, 162–175 (2013).
72. Q. Tseng, E. Duchemin-Pelletier, A. Deshiere, M. Balland, H. Guillou, O. Filhol, M. Thery, Spatial organization of the extracellular matrix regulates cell-cell junction positioning. *Proc. Natl. Acad. Sci. U.S.A.* **109**, 1506–1511 (2012).

Acknowledgments: We thank T. Bifano and J. J. Sun for providing microscope and technical support in Archon1 imaging. We thank A. Chopra and M. L. Kutys for helpful discussions and J. M. Finkelstein for suggestions on text editing. The WTC cell line (referred to as WT1) was provided by the Allen Institute for Cell Science Human iPSC Collection. **Funding:** This work was funded by the National Science Foundation Engineering Research Center on Cellular Metamaterials grant EEC-1647837 (to J.G.S., C.E.S., and C.S.C.), National Science Foundation Science and Technology Center for Engineering Mechanobiology grant CMMI-1548571 (to C.S.C.), National Institute of Health National Heart Lung and Blood Institute grant HL080494 (to J.G.S., C.E.S., and C.S.C.), American Heart Association Predoctoral Fellowship 17PRE33660967 (to K.Z.), American Heart Association Postdoctoral Fellowship 20POST35210045 (to S.S.), China Scholarship Council scholarship 201804910161 (to F.L.), National Science Foundation Graduate Research Fellowship DGE-1122374 (to S.L.D.) and DGE-1840990 (to J.K.E.), Boston University Presidential Scholarship (to S.T.), Sir Henry Wellcome Fellowship 206466/Z/17/Z (to C.N.T.), BHF CRE Intermediate Transition Fellowship RE/18/3/34214 (to C.N.T.), Leducq Foundation (to J.G.S. and C.E.S.), and Howard Hughes Medical Institute (to C.E.S.). **Author contributions:** Conceptualization and methodology: K.Z. and C.S.C. Investigation: K.Z., P.E.C., S.L.D., J.K.E., and J.L.B. Formal analysis and visualization: K.Z., P.E.C., F.L., S.T., J.L.B., and D.R. Software: S.S. and F.L. Cell line generation and sequencing: K.Z., C.N.T., J.D.C.M., and J.G. Supervision: J.G.S., C.E.S., and C.S.C. Writing: K.Z., J.E., J.G.S., C.E.S., and C.S.C. with input from all authors. **Competing interests:** J.G.S. and C.E.S. are founders and own shares in Myokardia Inc., a startup company that is developing therapeutics that target the sarcomere. C.S.C. is a founder and own shares of Innolign Biomedical, a company that is developing engineered organ models for pharmaceutical research and development, and Satellite Biosciences, a company that is developing cell-based therapies. The other authors declare that they have no competing interests. **Data and materials availability:** All data needed to evaluate the conclusions in the paper are present in the paper and/or the Supplementary Materials.

Submitted 10 March 2021
Accepted 25 August 2021
Published 15 October 2021
10.1126/sciadv.abh3995

Citation: K. Zhang, P. E. Cloonan, S. Sundaram, F. Liu, S. L. Das, J. K. Ewoldt, J. L. Bays, S. Tomp, C. N. Toepfer, J. D. C. Marsiglia, J. Gorham, D. Reichart, J. Eyckmans, J. G. Seidman, C. E. Seidman, C. S. Chen, Plakophilin-2 truncating variants impair cardiac contractility by disrupting sarcomere stability and organization. *Sci. Adv.* **7**, eabh3995 (2021).